Published in final edited form as:
Cell Rep. 2018 December 04; 25(10): 2676–2688.e7. doi:10.1016/j.celrep.2018.11.040.

tRNA Translocation by the Eukaryotic 80S Ribosome and the Impact of GTP Hydrolysis

Julia Flis[1], **Mikael Holm**[2], **Emily J. Rundlet**[2,3], **Justus Loerke**[1], **Tarek Hilal**[1], **Marylena Dabrowski**[1], **Jörg Bürger**[1,4], **Thorsten Mielke**[4], **Scott C. Blanchard**[2,3,*], **Christian M.T. Spahn**[1,5,*], and **Tatyana V. Budkevich**[1,*]

[1]Institut fur Medizinische Physik und Biophysik, Charité – Universitätsmedizin Berlin, Charitéplatz 1, 10117 Berlin, Germany

[2]Department of Physiology and Biophysics, Weill Cornell Medicine, New York, NY, USA

[3]Tri-Institutional PhD Program in Chemical Biology, Weill Cornell Medicine, New York, NY, USA

[4]UltraStrukturNetzwerk, Max Planck Institute for Molecular Genetics, 14195 Berlin, Germany

[5]Lead Contact

SUMMARY

Translocation moves the $tRNA_2$•mRNA module directionally through the ribosome during the elongation phase of protein synthesis. Although translocation is known to entail large conformational changes within both the ribosome and tRNA substrates, the orchestrated events that ensure the speed and fidelity of this critical aspect of the protein synthesis mechanism have not been fully elucidated. Here, we present three high-resolution structures of intermediates of translocation on the mammalian ribosome where, in contrast to bacteria, ribosomal complexes containing the translocase eEF2 and the complete $tRNA_2$•mRNA module are trapped by the non-hydrolyzable GTP analog GMPPNP. Consistent with the observed structures, single-molecule imaging revealed that GTP hydrolysis principally facilitates rate-limiting, final steps of translocation, which are required for factor dissociation and which are differentially regulated in bacterial and mammalian systems by the rates of deacyl-tRNA dissociation from the E site.

In Brief

Translocation, the process by which tRNA and mRNA are moved relative to the ribosome during protein synthesis, is facilitated in eukaryotic cells by the conserved GTPase elongation factor 2.

---

[*]Correspondence: scb2005@med.cornell.edu (S.C.B.), christian.spahn@charite.de (C.M.T.S.), tetyana.budkevych@charite.de (T.V.B.).

AUTHOR CONTRIBUTIONS
T.V.B., C.M.T.S., and S.C.B. designed the project. T.V.B. and M.D. prepared the 80S• $tRNA_2$•eEF2•GMPPNP complex. J.F., J.B., and T.M. collected the cryo-EM data. J.F., J.L., T.V.B., and C.M.T.S. carried out the image processing. J.F. and T.H. carried out the modeling. M.H. and E.J.R. collected and analyzed smFRET data. J.F., M.H., E.J.R., S.C.B., C.M.T.S., and T.V.B. discussed the results and wrote the paper.

DECLARATION OF INTERESTS
S.C.B. holds an equity interest in Lumidyne Technologies.

SUPPLEMENTAL INFORMATION
Supplemental Information includes six figures and two tables and can be found with this article online at https://doi.org/10.1016/j.celrep.2018.11.040.

Here Flis et al. combine cryo-EM and single-molecule FRET to elucidate features and intermediate states of translocation on mammalian ribosomes.

Graphical Abstract

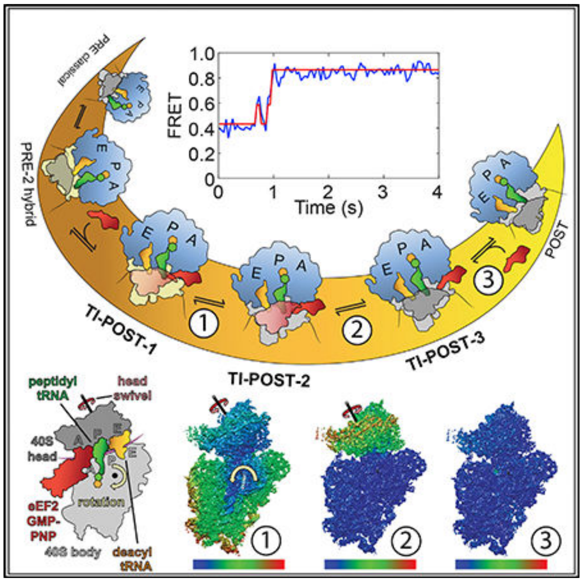

INTRODUCTION

Protein synthesis by the ribosome allows precise and reliable information transfer from mRNA to protein. The eukaryotic 80S ribosome (70S in bacteria) consists of a large 60S (50S in bacteria) and a small 40S (30S in bacteria) subunit. The large subunit contains the peptidyl transferase center (PTC) and the GTPase-activating center (GAC). The small subunit, consisting of the head and body/platform domains, contains the mRNA decoding center. The interface between the large and small subunits creates three tRNA binding sites: the acceptor (A), peptidyl (P), and exit (E) sites.

Protein synthesis occurs through processive elongation cycles (Melnikov et al., 2012; Voorhees and Ramakrishnan, 2013). At the beginning of each elongation cycle, an aminoacyl-tRNA in complex with eEF1A•GTP is selected on the basis of the mRNA codon at the A site of the post-translocation (POST) ribosome. Following accommodation of this tRNA, peptide bond formation transfers the nascent peptide chain from the P-site tRNA to the newly incorporated A-site tRNA to generate the pre-translocation (PRE) complex. To decode the subsequent mRNA codon, the intact $tRNA_2$•mRNA module must then be translocated with respect to the ribosome such that the two tRNAs together with the mRNA move from the A and P sites to the P and E sites, respectively.

During translocation, the ribosome must extensively remodel its contacts with the $tRNA_2$•mRNA module while keeping the mRNA codon-tRNA anticodon interactions intact to maintain the reading frame of translation (Noller et al., 2017). The capacity to translocate is initiated by deacylation of the P-site tRNA, which "unlocks" the ribosome (Valle et al., 2003), allowing the ribosomal subunits to spontaneously and reversibly rotate with respect to each other (Cornish et al., 2008). This rotation is coupled with the movement of tRNAs to intersubunit A/P and P/E hybrid states (Agirrezabala et al., 2008; Blanchard et al., 2004; Budkevich et al., 2011; Julián et al., 2008; Moazed and Noller, 1989; Munro et al., 2007).

Rapid translocation of the $tRNA_2$•mRNA module with respect to the small subunit on the rotated PRE complex requires the action of the GTPase eEF2 (EF-G in bacteria). eEF2 and EF-G both contain five conserved domains, including a ras-like G domain responsible for nucleotide binding and GTP hydrolysis (Bourne et al., 1991; Czworkowski et al., 1994). EF-G•GTP binds to the GAC of the 50S while contacting the anticodon-stem loop of peptidyl-tRNA. In bacteria, kinetic studies have suggested that GTP hydrolysis by EF-G occurs early in translocation and precedes tRNA movement on the small subunit (Rodnina et al., 1997). GTP hydrolysis accelerates translocation by as much as 50-fold, depending on the assay used (Ermolenko and Noller, 2011; Rodnina and Wintermeyer, 2011). The precise translocation mechanism and the role of GTP hydrolysis in the process remain active topics of research (Adio et al., 2015; Chen et al., 2013, 2016; Wasserman et al., 2016).

On bacterial ribosomes, translocation proceeds via translocation intermediate (TI)-PRE and TI-POST states. In the TI-PRE state, the small subunit is fully rotated (Brilot et al., 2013), whereas in the TI-POST state it is partially back-rotated with the 30S head swiveled in the direction of translocation relative to the 30S body/platform (Ramrath et al., 2013; Ratje et al., 2010; Zhou et al., 2014). The latter conformational change results in formation of chimeric (ap/P and pe/E) tRNA positions, in which deacyl- and peptidyl-tRNAs contact separate binding site elements on (1) the 30S head, (2) the 30S body, and (3) the 50S subunit, respectively. Current models of translocation posit that EF-G acts as a molecular “doorstop” that uncouples movement of the $tRNA_2$•mRNA module from the thermally driven backrotation of the 30S body/platform. The rate-limiting reverse swivel of the 30S head (Adio et al., 2015; Ermolenko and Noller, 2011; Ramrath et al., 2013; Ratje et al., 2010; Wasserman et al., 2016) then allows the tRNAs to move into their canonical P/P and E/E binding states (Gao et al., 2009). To continue with subsequent elongation cycles, EF-G•GDP must dissociate from the POST-translocation ribosome complex. We therefore operationally define completion of translocation as formation of a bona fide POST complex, which has a vacant A site. Correspondingly, EF-G-bound ribosome complexes are translocation intermediates, even if the tRNAs have already reached their POST positions.

Despite extensive evolutionary conservation of the core translation machinery, bacterial and eukaryotic initiation, termination, and recycling phases of protein synthesis are facilitated by nonhomologous translation factors (Melnikov et al., 2012). For instance, eukaryotic translational control mechanisms exploit alternative modes of translation initiation, driven by *cis*-acting internal ribosome entry sites (IRESs) (Jackson et al., 2010; Yamamoto et al., 2017). Functional differences between bacterial and eukaryotic translation elongation are also likely given the physically distinct nature of the tRNA binding sites in these systems (Behrmann et al., 2015; Budkevich et al., 2011), which likely impinge on ribosomal intersubunit dynamics (Ferguson et al., 2015), including subunit rolling (Budkevich et al., 2014). In contrast to what is observed in bacteria, the E site of the mammalian 60S subunit remains occupied by a deacyl-tRNA during all steps of translation elongation (Behrmann et al., 2015). Disparities in the translation mechanism are further evidenced by the species-dependent antibiotic sensitivities of bacterial and mammalian ribosomes (Wilson, 2009) and the existence of additional species-specific translation elongation factors (Andersen et al., 2006).

Cryo-electron microscopy (cryo-EM) structures have been obtained of eukaryotic ribosomes bound to eEF2 (Anger et al., 2013; Pellegrino et al., 2018; Spahn et al., 2004; Taylor et al., 2007; Voorhees et al., 2014). However, these structures do not contain the complete $tRNA_2$•mRNA module, hampering insights into the mechanism of canonical translocation. High-resolution structures of yeast ribosomes during the translocation of type IV IRESs, which mimic components of the $tRNA_2$•mRNA module, have also been obtained (Abeyrathne et al., 2016; Murray et al., 2016). However, it is not clear to what extent type IV IRES translocation resembles $tRNA_2$•mRNA translocation. Here, we present cryo-EM structures of the rabbit 80S•$tRNA_2$•eEF2•GMPPNP complex together with single-molecule fluorescence resonance energy transfer (smFRET) investigations that reveal bona fide intermediate states of canonical translocation on the eukaryotic ribosome. Surprisingly, during both bacterial and eukaryotic translocation, we find that GTP hydrolysis primarily affects the resolution of late intermediates of translocation that occur after movement of the $tRNA_2$•mRNA module with respect to the ribosome. We also find that the mechanisms of bacterial and eukaryotic translocation are distinguished principally by the rate and timing of deacylated tRNA dissociation from the E site, which regulates reversibility of the rate-limiting progression to the POST complex.

RESULTS AND DISCUSSION

Cryo-EM Analysis of Mammalian Translocation Intermediates

To visualize TI states of the mammalian 80S ribosome, we prepared translocating ribosomes *in vitro*, using purified components, in the presence of the non-hydrolyzable GTP analog GMPPNP (STAR Methods). Briefly, PRE complexes were formed from programmed mammalian 80S ribosomes with P-site deacyl-$tRNA^{Phe}$ and A-site N-acetyl-Val-$tRNA^{Val}$. Incubation with eEF2•GMPPNP led to stalling of eEF2 on the 80S ribosome. The 80S•$tRNA_2$•eEF2•GMPPNP complex was subjected to multi-particle cryo-EM analysis (Loerke et al., 2010), resulting in an ensemble of three different reconstructions of 80S TI states and respective atomic models with global resolution ranging from 3.5 to 3.6 Å and local resolution of up to 3.2 Å in the core regions of the ribosomal subunits (Figure S1; Table S1). Each cryo-EM map shows clear electron density for both the complete $tRNA_2$•mRNA module and eEF2. As expected, peripheral, flexible components are less well resolved. In each complex, the $tRNA_2$•mRNA modules are largely translocated with respect to the 60S subunit and the 40S body/platform (Figure 1), indicative of TI-POST-like translocation intermediates. Differences in the observed conformations of the 40S domains and in the exact positions of the tRNAs and the L1 stalk allowed us to arrange the reconstructions sequentially along the translocation reaction coordinate as TI-POST-1, TI-POST-2 and TI-POST-3 intermediate states of translocation (Figures 1 and 2).

Late Intermediates of Mammalian Translocation Are Distinguished by 40S Body/Platform Rotation and 40S Head Swivel

The first translocation intermediate, TI-POST-1, has a partially rotated 40S subunit (~4°) and a highly swiveled 40S head (~18°) compared with the mammalian POST state (Behrmann et al., 2015) (Figure 2A). As in the bacterial TI-POST complex (Ramrath et al., 2013; Zhou et al., 2014), tRNAs occupy chimeric ap/P and pe/E hybrid positions, defined by signature interactions of the tRNA anticodon-stem loops. These include ap/P tRNA contacts with C1701 (40S body/platform P site, *E. coli* C1400) and C1331 (40S head A site, *E. coli* A1054), and pe/E tRNA contacts with U1248 (40S head P site, *E. coli* G966) and G961 (40S body/platform E site, *E. coli* G693) (Figures 3A, 3B, S3A, and S3B). Consistent with what has been observed in bacteria (Mohan and Noller, 2017; Zhou et al., 2013), the L1 stalk leans toward the E-site tRNA such that the L1 stalk bases G3929 (*E. coli* G2112) and A4016 (*E. coli* A2169) of 28S rRNA helix 77 (H77) stack onto bases G19 and C56 of the pe/E tRNA elbow (Figures S2A and S2B).

In the transition from the TI-POST-1 to the TI-POST-2 state, the 40S subunit rotates backward by 3.5° around an axis through RACK1 and eL41 (Figure 2B) such that the 40S body/platform closely resembles the classical POST state (~0.7° residual rotation) (Figure 2C). Interestingly, the 40S head domain only partially follows back-rotation of the 40S body/platform (1.9°instead of 3.5°; Figure 2B), resulting in modest exaggeration of the 40S head swivel motion (~19°). As the 40S components in contact with the tRNAs display minimal movement due to proximity to the axis of subunit rotation (Figure 2B), both tRNAs maintain chimeric hybrid state interactions (Figure S2C). The mammalian TI-POST-2 structure therefore represents a previously uncharacterized intermediate between the bacterial TI-POST with chimeric hybrid tRNAs (Ramrath et al., 2013; Zhou et al., 2014) and the 70S•tRNA•EF-G•fusidic acid complex in the classical, POST conformation (Gao et al., 2009).

The 40S body/platform rotates further backward in the transition to TI-POST-3, rendering its position indistinguishable from that of the classical POST state (Figures 2D and 2E). The tRNAs in the TI-POST-3 complex now establish classical P/P and E/E interactions, and the L1 stalk adopts the same position as in the mammalian (Behrmann et al., 2015) and bacterial (Mohan and Noller, 2017) POST states (Figures S2A and S2D). The 40S head also swivels back to its classical position. Notably, however, the 40S head exhibits a residual tilt in the TI-POST-3 complex (~1° perpendicular to the 40S head swivel axis) (Figure 2E), a feature that distinguishes it from the classical POST complex.

All three mammalian translocation intermediates, including the existence and conformation of TI-POST-2, are congruent with our recent smFRET investigations of translocation on the bacterial ribosome (Wasserman et al., 2016). These structures reveal two distinct late steps of translocation on the mammalian ribosome in which the 40S body/platform first reverse rotates (Figure 2B), followed by reverse swivel of the 40S head (Figure 2D). The 40S head swivel and 40S body/platform rotation observed in TI-POST-1 and TIPOST-2 result in a maximal ~28 Å opening of the P gate, a constriction between the A1641 (*E. coli* A1340) residue of the 40S head and the A1058 (*E. coli* A790)residue within the 40S body/platform that restricts P-site tRNA entry into the small subunit E site in classical ribosome configurations (Schuwirth et al., 2005) (Figures 2F–2K; Table S2). From the perspective of the 60S subunit, the overall tRNA positions do not substantially change in the TI-POST-1 to TI-POST-3 transition. Thus, rather than the P-site tRNA moving through the gate, the observed motions suggest that conformational changes within the 40S subunit move the P gate around the deacyl-tRNA during the penultimate steps of translocation.

ComparisonoftRNATranslocationwithTranslocationof Viral Type IV IRES RNAs

Two independent studies have recently investigated the structural basis of viral type IV IRES translocation in yeast by stalling eEF2 with GMPPCP (Murray et al., 2016) or the antibiotic sordarin (Abeyrathne et al., 2016). These studies established that IRES translocation, like canonical tRNA translocation, requires a sequence of global conformational changes within the ribosome, including intersubunit rotation and head swivel. However, comparison with the present structures of intermediate states of canonical tRNA translocation shows several notable distinctions with regard to the energy landscape and reaction coordinate of translocation. Contrary to the present three TI-POST intermediates, the IRES study using GMPPCP identified a single early intermediate resembling a TI-PRE state (Murray et al., 2016). This distinction likely stems from the lack of critical interactions with the ribosome, such as those formed by the P-site deacyl-tRNA and the 3′-CCA end of A-site peptidyl-tRNA with the PTC.

The five 80S•IRES•eEF2•sordarin states captured (Abeyrathne et al., 2016) are also conformationally distinct to some extent from those reported here. Although the conformation of the 80S•IRES•eEF2•sordarin state II complex resembles the TI-POST-1 state (Table S2), the next intermediate does not exhibit back-rotation/back-rolling of the 40S body/platform, and this study did not reveal an intermediate that combines negligible 40S body/platform rotation and maximal head swivel as seen in the TI-POST-2 state. In addition, it is unlikely that the conformation observed in state IV of the 80S•IRES•eEF2•sordarin complex (Abeyrathne et al., 2016) is relevant to translocation of a $tRNA_2$•mRNA module, as the 40S head would clash with the E-site tRNA. Moreover, in both studies, the L1 stalk is occluded from the E site by elements of the IRES (Figure S2). Thus, although there are overall similarities, the nature of conformational changes within the ribosome during IRES translocation appears to be distinct from that of canonical translocation.

The Role of eEF2 Domain IV during Translocation

Structures of bacterial TI-POST states suggest that a major function of EF-G is to prevent backward movement of the $tRNA_2$•mRNA module during back-rotation of the 30S body/platform (Ramrath et al., 2013; Zhou et al., 2014). Domain IV of EF-G, which is principally responsible for this “doorstop” function, contains the functionally important loops 1, 2, and 3 (Czworkowski et al., 1994). eEF2 adopts a similar architecture to EF-G but possesses the unique diphthamide post-translational modification on histidine 715 of domain IV loop 3 (Oppenheimer and Bodley, 1981). In all three structures, domain IV of eEF2 reaches into the interface of the 40S body/platform and 40S head, targeting the peptidyl-tRNA codon-anticodon interaction (Figure 3C). Comparison of our mammalian TI-POST structures with a bacterial TI-POST state (Zhou et al., 2014) reveals that loop 1 is shorter in eEF2 than in EF-G (Figure 3C). Interestingly, density at low contour levels (Figure 3E) indicates that the diphthamide residue protrudes from the neighboring loop 3 into the space left by the shorter loop 1 of eEF2, where it packs against the ribose of A36 of the peptidyl-tRNA (Figure 3C). In the context of eEF2's "doorstop" function, the diphthamide modification may restrict movements of peptidyl-tRNA during translocation, consistent with its role in suppressing −1 frameshifting (Ortiz et al., 2006).

Loop 3 of eEF2 domain IV approaches 18S rRNA h44, which contains the so-called monitoring bases, A1824 and A1825 (*E. coli* A1492 and A1493) (Figures 3C, 3D, 3F, S3C, and S3D), which extrude from h44 to form A-minor interactions with the codon-anticodon duplex in the A site (Ogle et al., 2002; Selmer et al., 2006). In our structures, A1825 but not A1824 extrudes from h44 (Figures 3D, 3F, S3C, and S3D), likely stabilized by A3731 of the 28S rRNA (*E. coli* A1913), which participates in the formation of bridge B2a by protruding into the decoding loop (Figure 3F). A1825 is sandwiched between the first base of the new A-site codon and a glycine-triplet (G717–G719) at the N terminus of helix B of eEF2 domain IV (Figures 3D and S3C). The extruded A1825 on the 5′ end and 18S rRNA C1698 on the 3′ end appear to be involved in stacking interactions with the downstream mRNA codon (bases +4 to +6) and mRNA base +7 (Figures 3D and S3C). This mRNA position and conformation is similar to that observed in the presence of an A-site tRNA making codon-anticodon interactions (Selmer et al., 2006; Zhou et al., 2013). Clamping the upstream part of the mRNA and enforcing a stacked arrangement of mRNA nucleotides in the A site could serve to maintain the reading frame and to prime the mRNA for the next round of tRNA selection to ensure unimpeded elongation.

The G-Domain of eEF2 Is in the Active GTP Conformation in All Three Translocation Intermediates

The conformation of eEF2 and its position with respect to the 60S subunit is largely invariant in the TI-POST-1 to TI-POST-3 states. The G domain of eEF2 is bound to the GAC of the 60S subunit that contains the P1/P0 stalk base and the sarcin-ricin loop (SRL; H95 of 28S rRNA) (Figure 4A). The G-domain conformation in our GMPPNP-stalled intermediates resembles previous structures of EF-G and eEF2 with GTP or GMPPCP in the pre-hydrolysis, GTP state (Connell et al., 2007; Murray et al., 2016; Pulk and Cate, 2013; Tourigny et al., 2013; Zhou et al., 2013). As expected for an activated state, we observe ordered density for switch I (Figure 4B), and histidine 108 of switch II is flipped toward the γ-phosphate of GMPPNP and the tip of the SRL (Figures 4A–4C).

Attempts to visualize bacterial translocation intermediates containing two tRNAs using GMPP(N/C)P have been unsuccessful (discussed in Gao et al., 2009, and Penczek et al., 2006). Thus far, they have led to structures containing only a single pe/E- or P/E-site tRNA or lacking tRNA altogether (Connell et al., 2007; Pulk and Cate, 2013; Tourigny et al., 2013; Zhou et al., 2013). Structural investigations of TI states have instead required EF-G•GDP stabilization on the ribosome by the antibiotic fusidic acid (Brilot et al., 2013; Gao et al., 2009; Ramrath et al., 2013; Zhou et al., 2014). Our capacity to obtain structures of 80S•tRNA$_2$•eEF2•GMPPNP therefore suggests fundamental differences between mammalian and bacterial translocation mechanisms.

GTP Hydrolysis Is Principally Required for Late Steps in the Translocation Mechanism

To investigate the effects of GMPPNP on translocation of the mammalian ribosome, we used smFRET to monitor distance changes between A- and P-site tRNAs (Figures 5A–5C). Human PRE complexes containing A-site Cy5-labeled Met-PhetRNA^{Phe} and P-site Cy3-labeled tRNA^{fMet} were prepared as described previously (Ferguson et al., 2015). Translocation was initiated by stopped-flow delivery of eEF2 together with either GTP (Figure 5B) or GMPPNP (Figure 5C). As expected, prior to eEF2 addition, human PRE complexes predominantly occupied intermediate-FRET (0.43 ± 0.06) states, previously identified as hybrid state pre-translocation complexes (Ferguson et al., 2015). Upon addition of either eEF2•GTP or eEF2•GMPPNP, the ribosome rapidly proceeded to a high-FRET (0.86 ± 0.05) state via at least one shortlived intermediate-FRET (0.55 ± 0.05) state, consistent with translocation being accompanied by sequential tRNA compaction steps (Figures 5A–5C). The nucleotide identity had only modest effects on the mean time of this process, estimated as 1.0 ± 0.15 s with GTP and 2.3 ± 0.3 s with GMPPNP (Figure S4A).

As expected for the thermodynamically stable POST state (Ferguson et al., 2015), ribosomes translocated by eEF2•GTP remained in the high-FRET state after eEF2•GTP was removed from the imaging chamber by buffer exchange (Figures 5B and S4B). Surprisingly, for ribosomes translocated with eEF2•GMPPNP this washout procedure led to a slow reversion to intermediate FRET (mean time 350 ± 75 s), consistent with slow release of eEF2•GMPPNP from the ribosome and return of the 80S complex to a rotated, hybrid state conformation (Figures 5C and S4C). This assignment was confirmed by translocating these reversed complexes with eEF2•GTP, which resulted in irreversible POST complex formation (Figure S4D). These results, which show that translocation is not completed in the presence of GMPPNP, are consistent with a recent study (Susorov et al., 2018) showing that both eEF2•GMPPNP and eEF2•GTP are capable of catalyzing reverse translocation under specific experimental conditions. Together with our cryo-EM structures, these findings demonstrate that early steps of translocation, during which the inter-tRNA distances change, are largely unaffected by GMPPNP, while late steps of translocation, which structurally resemble TI-POST-1, TI-POST-2, or TI-POST-3 with regard to tRNA positioning, are stalled.

For comparison with bacterial translocation, we carried out the same experiments using bacterial PRE complexes and EF-G. Upon delivery of EF-G with either GTP or GMPPNP, the bacterial ribosome proceeded rapidly from the intermediate-FRET (0.46 ± 0.08) rotated PRE state to a short-lived, high-FRET (0.75 ± 0.05) state, consistent with tRNA compaction, followed by loss of the FRET signal due to dissociation of the E-site tRNA (Figures 5D– 5F) (Wasserman et al., 2016). The mean transit times of these events were similar using GTP or GMPPNP (Figure S4E), consistent with GMPPNP having negligible effects on the rates of translocation events preceding deacyl-tRNA release from the bacterial ribosome. These findings collectively suggest that the free energy of eEF2/EF-G binding in GTP-bound conformations to the PRE-state ribosome is sufficient to drive rapid formation of TI-POST states on both mammalian and bacterial ribosomes.

To determine whether inhibiting GTP hydrolysis affects resolution of late steps of translocation in bacteria, we used an alternative structural perspective on translocation that reports on the relative distance between A-site peptidyl-tRNA and the N terminus of ribosomal protein uS13 in the 30S head (Figure 6A) (Wasserman et al., 2016). Prior to translocation, the ribosome predominantly occupied a low-FRET (0.19 ± 0.03) state, consistent with the large distance between the peptidyl-tRNA in the A site and uS13 within a rotated ribosome configuration. Stopped-flow delivery of EF-G•GTP resulted in rapid transition to a short-lived, intermediate-FRET (0.28 ± 0.03) state, identified as TI-POST-1, followed by progression to a higher intermediateFRET (0.48 ± 0.05), classical POST state (Figure 6B) (Wasserman et al., 2016). This reaction sequence was readily visualized in transition density plots (TDPs) of the ensemble of individual molecules examined (Figure 6C) (McKinney et al., 2006). As previously described (Alejo and Blanchard, 2017; Wasserman et al., 2016), the POST-state ribosome achieved a stable equilibrium between intermediate-FRET (0.48 ± 0.05) and high-FRET (0.78 ± 0.05) states (Figure 6B). The intermediate-FRET state reflects the expected conformation of the system after translocation: classically positioned P/P tRNA on the unrotated ribosome. The POST complex’s transition to a high-FRET state conformation indicates a decrease in distance between the peptidyl-tRNA elbow and uS13. Such a state is consistent with a P/E-like peptidyl-tRNA position, presumably accompanied by rotation of the small ribosomal subunit (Alejo and Blanchard, 2017). In line with this assignment, peptide release by puromycin dramatically shifted the equilibrium toward the high-FRET state (Figure S5A). Peptidyl-tRNA excursions to a hybrid-like position within the POST-translocation ribosome are likely enabled by E-site vacancy and EF-G binding.

When the bacterial ribosome was translocated in the presence of GMPPNP, we observed strikingly different behaviors (Figures 6D and 6E). Specifically, the overall lifetime of the TI-POST-1 state (0.28 ± 0.03 FRET) was extended more than 50-fold (Figure 6D). Strikingly, inspection of individual smFRET traces on path to complete translocation revealed that the GMPPNPstalled transition from the TI-POST-1 state featured reversible transitions to higher FRET, POST-like configurations (Figure 6E). This unexpected finding suggests that non-productive translocation attempts can precede completion of translocation. Reversibility at this step is also clearly evidenced in TDPs, which exhibit near symmetric transition frequencies with respect to the diagonal (Figure 6E). These data suggest that the primary role of GTP hydrolysis on the bacterial ribosome is to irreversibly trap the POST complex once it has formed.

Notably, although the bacterial ribosome slowly translocated in the presence of GMPPNP, ultimately reaching the same FRET states observed in the presence of GTP, the high-FRET (0.78 ± 0.05) POST-state conformation predominated at equilibrium (Figure 6D). This altered equilibrium persisted while EF-G•GMPPNP was present in the flow cell. In stark contrast to experiments on the mammalian ribosome (Figures 5A–5C), E-FG•GMPPNP washout from the flow cell did not lead to reversion to the PRE state but instead generated a ribosome complex that was indistinguishable from the canonical POST complex obtained with EF-G•GTP (Figures 6 and S5B). Addition of EF-G•GMPPNP to fully translocated POST ribosomes rapidly returned the system to the high-FRET state (Figure S5C), in line with the established kinetics of EF-G•GMPPNP binding (Munro et al., 2010a).

Taken together, these findings reveal that EF-G•GMPPNP dramatically and specifically impedes very late steps of translocation. In the GMPPNP-stalled bacterial complex, reversible exchange between late intermediates, akin to the TI-POST-1, TI-POST-2, and TI-POST-3 states captured by our cryo-EM studies of the mammalian ribosome, ultimately gives rise to complete translocation and stabilization of a predominantly rotated ribosome conformation in which EF-G•GMPPNP is bound. We conclude that EF-G•GMPPNP binding to POST complexes lacking an E-site tRNA is sufficient to overcome interactions of the 3′-CCA end of peptidyl-tRNA bearing short nascent peptides with the 50S P site to promote a hybrid-like tRNA position. Further experiments will be required to determine the extent to which such propensities are dampened by longer nascent peptides.

Conclusions

The three distinct intermediate states of mammalian translocation described here indicate that events prior to the rate-limiting barrier crossing event that completes translocation are facilitated by progressively larger interaction energies between eEF2 and the ribosome (reviewed in Spirin, 2009). Together with our previous structures of mammalian PRE- and POSTstate ribosomes (Behrmann et al., 2015; Budkevich et al., 2011), the present findings indicate that these eEF2 interactions enable nearly complete movement of the $tRNA_2$•mRNA module with respect to the ribosome prior to GTP hydrolysis (Figure 7).

Prior to eEF2 binding to the rotated PRE-2 complex, A/P and P/E hybrid state tRNAs have already covered a major portion of the distance toward their final P/P and E/E positions, especially relative to the 60S subunit. Because of internal tRNA conformational changes, the tRNA bodies, but not the anticodon-stem loops, have also moved a significant distance relative to the 40S body/platform in the direction of translocation (Figure 7). By analogy with bacterial translocation, we propose that initial binding of eEF2 results in a TI-PRE state with large intersubunit rotation and little to no 40S head swivel (Brilot et al., 2013). Although the structure of such a state has yet to be solved, the transient FRET state (0.55 ± 0.05) observed on the path to POST complex formation during the initial steps of translocation (Figures 5A–5C) supports the existence of one or more such TI-PRE states during translocation of the mammalian ribosome.

Back-rotation and back-rolling, together with the swivel-like motion of the 40S head, provide a significant shift of the $tRNA_2$•mRNA module relative to the 60S subunit and the 40S body/platform in the direction of translocation, resulting in compacted TI-POST-1 chimeric ap/P and pe/E hybrid states (Figure 7). Accordingly, the axis of 40S back-rotation in the presence of eEF2 is different from that observed in the transition between unrotated and rotated PRE states as the formation of the TI-POST-1 state combines back-rotation with 3° of subunit back-rolling (Budkevich et al., 2014) (Figure S6). In contrast, the transition from TI-POST-1 to TI-POST-2 results in only minor changes in the tRNA positions (Figure 7). The same is true for the transition from TI-POST-2 to TI-POST-3, where the $tRNA_2$•mRNA module is translocated relative to the 40S head by reverse swivel. Notably, we find that GTP hydrolysis contributes only modestly to the dramatic, initial movements of the $tRNA_2$•mRNA module, while profoundly affecting the rate-determining steps responsible for resolving the rapidly formed TI-POST complexes to the bona fide POST state by facilitating eEF2 dissociation (Figures 5 and 6).

Although resolution of these late-intermediate states of translocation is slowed by roughly 50-fold in the absence of GTP hydrolysis, the bacterial ribosome is able to complete translocation in the presence of EF-G•GMPPNP. By contrast, the mammalian ribosome is either unable to achieve the bona fide POST state in the absence of GTP hydrolysis or final steps of translocation are slowed to an extent that is beyond our present capabilities to determine with precision (i.e., more than 2,000-fold). As our mammalian and bacterial ribosome translocation experiments were performed under identical conditions, these findings suggest a large and unexpected functional difference in the otherwise highly conserved elongation mechanism. We hypothesize that this apparent divergence is likely explained by the marked differences in E-site tRNA occupancy within the POST-like intermediate states of bacterial and mammalian ribosomes. In bacteria, dissociation of deacyl-tRNA from the E site prior to POST complex formation renders the reversal of translocation highly unfavorable. E-site tRNA dissociation also allows transient excursions of the bacterial ribosome to a rotated state in which peptidyl-tRNA can adopt a hybrid-like position. However, the contributions of such conformations to the completion of translocation remain to be determined. The presence of deacyltRNA on the mammalian ribosome throughout and subsequent to translocation appears to further slow the completion of translocation in the absence of GTPase activity. Such observations are consistent with marked structural and kinetic, distinctions between mammalian and bacterial translocation mechanisms (Ferguson et al., 2015).

We conclude from the data obtained that formation of POST-like ribosome conformations facilitates the transitions of EF-G and eEF2 to their GDP conformations to trigger their dissociation from the ribosome; the terminal step in the translocation mechanism. Such a model is reminiscent of proposed activities of other soluble GTPases (Inoue-Yokosawa et al., 1974).

STAR⋆METHODS

CONTACT FOR REAGENT AND RESOURCE SHARING

Further information and requests for resources should be directed and will be fulfilled by the Lead Contact, Christian M.T. Spahn (christian.spahn@charite.de).

EXPERIMENTAL MODEL AND SUBJECT DETAILS

E. coli* strains DH10B, BL21(DE3) and MRE600—E. coli* strain DH10B (ThermoFisher Scientific) was used for DNA plasmid amplifications. The strain was grown in LB-medium or on LB-agar with or without antibiotics which the strain is naturally resistant to (tetracycline or chloramphenicol) or (if transformed) which the strain obtained resistance to by plasmid uptake (either ampicillin or kanamycin).

E. coli strain BL21-CodonPlus (DE3)-RIPL (ThermoFisher Scientific) was used for preparation of recombinant proteins. The strain is tetracycline resistant and was grown either in LB-medium or on LB-agar with either tetracycline or other antibiotics (resistance acquired by through plasmid transformation).

E. coli strain MRE600 (ATCC) was used for ribosome preparation. It was grown in LB media or on LB agar plates without antibiotic. All bacterial strains were grown at 37, 25 or 18°C as required.

HEK293 T cell line—HEK293T cells (ATCC CRL-3216) were grown in Dulbecco's Modified Eagle Medium (DMEM) (Sigma-Aldrich) supplemented with 10% Fetal Bovine Serum (FBS) (GIBCO) and penicillin-streptomycin (100 U/ml, GIBCO) at 37 °C with 5% CO_2. Absence of mycoplasma contamination confirmed by MycoAlert Mycoplasma Detection Kit.

METHOD DETAILS

Preparation of mammalian (rabbit, human) and bacterial ribosomal subunits— Ribosomal subunits (40S and 60S) from rabbit reticulocyte lysate (RRL; Green Hectares), free of endogenous tRNAs and mRNAs used for cryo-EM sample preparation were prepared according to (Bommer et al., 1997). Ribosomes were sedimented from 300 mL of nuclease treated RRL in a 50.2 Ti rotor (Beckman Coulter) at 40,000 rpm for 3 h at 4°C. The pellets were briefly washed and resuspended in buffer; 5 mM HEPES pH 7.5, 50 mM KCl, 1.5 mM $MgCl_2$, 2 mM DTT using a glass dounce with Teflon pestle. The ribosome concentration was about 20 mg/ml as judged by A_{260}. The KCl concentration was adjusted to 0.5 M. Freshly prepared puromycin (1 mg/ml) was added to give a ratio of 1 mg puromycin per 100 mg of ribosomes. The final ribosome concentration was adjusted to 10 mg/ml while maintaining 0.5 M KCl. Ribosomes were incubated 30 min on ice and 15 min at 37°C. Dissociated subunits were layered on 10%–30% linear sucrose gradients in buffer; 5 mM HEPES pH 7.5, 500 mM KCl, 5 mM $MgCl_2$, 2 mM DTT and centrifuged in a swinging-bucket rotor (SW32 Beckman Coulter) at 18,000 rpm for 18 h at 4°C. The gradients were fractionated while monitoring A_{260}. The main fractions of the 40S and 60S peaks were pooled, avoiding the overlapping area. The pooled fractions were diluted 1:1 with buffer; 50 mM HEPES pH 7.4, 30 mM $MgCl_2$, 2 mM DTT and ribosomes were pelleted down by centrifugation in a Type 45 Ti rotor (Beckman Coulter) at 40,000 rpm for 18 h at 4°C. Ribosome pellets were resuspended in 20 mM HEPES pH 7.4, 50 mM KCl, 2 mM $MgCl_2$, 1 mM DTT. The purified subunits were frozen in liquid nitrogen and stored at −80°C. Re-association to 80S ribosomes was confirmed by analytical centrifugation in a SW40 rotor (Beckman Coulter) at 18,000 rpm, 18 h. Ribosome concentrations were calculated assuming the following ratios: 60 pmol/A_{260} for 40S subunits, 30 pmol/A_{260} for 60S subunits and 20 pmol/A_{260} for 80S ribosomes.

Ribosomal subunits from human tissue culture (HEK293T) used for smFRET experiments were purified essentially by the same method (Bommer et al., 1997). Specific deviations are described in (Ferguson et al., 2015).

Wild-type 30S and 50S ribosomal subunits were purified from *E. coli* MRE600 and used to prepare initiation complexes as previously described (Blanchard et al., 2004). uS13-labeled 30S subunits were prepared as previously described (Wasserman et al., 2015).

Preparation of mammalian and bacterial elongation factors—Elongation factors eEF1A and eEF2 were isolated from rabbit reticulocyte lysate (RRL; Green Hectares) using a protocol modified from (Pestova and Hellen, 2003). Using a sucrose cushion (1 M sucrose, 500 mM KCl, 5 mM $MgCl_2$, 20 mM TRIS-HCl pH 7.5, 1 mM Dithiothreitol (DTT), 20% glycerol), RRL was clarified of ribosomes by ultracentrifugation (Type 45 Ti Rotor, Beckman Coulter) spun at 40,000 rpm for 14 h at 4°C in the presence of high salt (500 mM KCl), 1 mM phenylmethane sulfonyl fluoride (PMSF), and Mammalian ProteaseArrest (G-Biosciences). The resulting supernatant was subjected to ammonium sulfate precipitation and eEF1A and eEF2 were further purified from the 30%–40% and 50%–60% ammonium sulfate fractions, respectively. Both fractions were dialyzed overnight into Buffer A1 (50 mM KCl, 20 mM TRIS-HCl pH 7.5, 1 mM DTT, 0.1 mM EDTA, 20% glycerol) and passed over a HiPrep DEAE FF 16/10 chromatography column (GE Healthcare Life Sciences). eEF1A, collected from the flow-through fraction, was purified over a HiTrap SP HP chromatography column using a 50–300 mM KCl gradient, dialyzed into Buffer A1 and further purified using a Mono S 5/50 GL chromatography column (GE Healthcare Life Sciences) and eluted using a 50–200 mM KCl gradient. Purified eEF1A was dialyzed overnight against eEF1A storage buffer (25 mM KCl, 20 mM TRIS-HCl pH 7.5, 5 mM MgOAc, 6 mM β-mercaptoethanol, 60% glycerol) and stored at −20 °C.

eEF2 was eluted from the DEAE column using a 50–300 mM KCl gradient and dialyzed overnight against Buffer A2 (50 mM KCl, 20 mM HEPES pH 6.1, 1 mM DTT, 0.1 mM EDTA, 20% glycerol). For cryo-EM study the fraction containing eEF2 was further purified using P11 phosphocellulose (Sigma-Aldrich) using 50–500 mM KCl gradient. For FRET experiments a HiTrap Heparin HP chromatography column (GE Healthcare Life Sciences) and elution using a 50–500 mM KCl gradient was used. After dialysis against Buffer A1 the fraction containing eEF2 was further purified and concentrated using a Mono Q 5/50 GL chromatography column (GE Healthcare Life Sciences) and eluted using a 50–300 mM KCl gradient. The purified eEF2 was then dialyzed against human polymix buffer (30 mM HEPES pH 7.5, 5 mM $MgCl_2$, 50 mM NH_4Cl, 2 mM spermidine, 5 mM Putrescine, 1.5 mM β-mercaptoethanol) (Ferguson et al., 2015) containing 5% glycerol, flash frozen and stored in liquid nitrogen.

EF-Tu, the bacterial homolog of eEF1A, was purified as previously described (Burnett et al., 2014). EF-G, the bacterial homolog of eEF2, was purified as previously described (Munro et al., 2010b).

Preparation of radioactively-labeled rabbit tRNA^{Val}—Total tRNA was obtained from 1 L of postribosomal supernatant according to an acid phenol extraction method described (Rogg et al., 1969). Eukaryotic tRNA^{Val} was purified according to (Miyauchi et al., 2007). A synthetic 3′-biotinylated DNA probe (5′-TgTTTCCgCCCggTTTCgAACCggggACCT-BIO-3′) was designed to be complementary to the 3′-terminal segment of eukaryotic tRNA^{Val}, mixed with streptavidin Sepharose resin (GE Healthcare Life Sciences) in 6X saline-sodium citrate (SSC) buffer (900 mM NaCl, 90 mM Na citrate (adjusted to pH 7.0 with HCl)) and incubated 7 min at 65°C. Unbound material was collected by short (few seconds) low speed centrifugation (1,000 rpm). Extensive washing was done by 3X SSC buffer until optical density of the washed solution at A_{260} was below 0.05. Elution was performed by mixing of resin with 0.1 X SSC buffer pre-heated at 65°C, incubating 5 min at 65°C, and short (few seconds) low speed centrifugation (1,000 rpm). The elution cycle was repeated 6–7 times. Eluted fractions were precipitated by 3 volumes of ethanol. Amino acid acceptor activity was determined by incubation of 0.1 A_{260} units of purified $tRNA^{Val}$, 900 pmol of $[^{14}C]$Val (600 dpm/pmol) and 5 A_{280}/ml of total aminoacyl-tRNA synthetases (ARSases) in a 50 μl reaction mixture (30 mM HEPES pH 7.6, 100 mM KCl, 5 mM $MgCl_2$, 3 mM ATP, 1 mM DTT). The amount of aminoacylated tRNA was determined by cold TCA precipitation after 15 min incubation at 37°C. Control incubation in the absence of tRNA was performed to set the filter background.

Acetyl-$[^{14}C]tRNA^{Val}$ was obtained by incubation of 150 μg deacylated $tRNA^{Val}$ in 400 μl containing 30 mM HEPES pH 7.6, 100 mM KCl, 5 mM $MgCl_2$, 3 mM ATP, 1 U/μl RNasin® Plus (Promega), 1 mM DTT, 60 μM $[^{14}C]$Val, 600 dpm/pmol (PekinElmer) and 5 A_{280}/ml ARSases for 15 min at 37°C. After phenol/chloroform/isoamyl alcohol extraction, an acetylation step on ice in the presence of acetic anhydride was performed. 1/30 volumes of acetic anhydride was added to the $[^{14}C]$Val-tRNA mix every 15 min a total of 4 times. Deacylation was performed in 400 μl containing 30 mM HEPES pH 7.6, 100 mM KCl, 5 mM $MgCl_2$, 1 U/ml RNasin Plus (Promega), 1 mM DTT, 5 A_{280}/μ®l total aminoacyl-tRNA synthetases, 6 mM AMP and 6 mM pyrophosphate (PP_i) for 5 min at 30°C. After another round of phenol/chloroform/isoamyl alcohol extraction N-acetyl-$[^{14}C]Val\text{-}tRNA^{Val}$ was purified by reversed-phase HPLC on a Nucleosil 300–7 C8 HPLC column (Knauer) using a methanol gradient as described (Triana et al., 1994). After each step of the purification the amount of charged material was determined by TCA precipitation.

Cryo-EM sample formation—To obtain 80S•$tRNA_2$•mRNA•eEF2•GMPPNP complex, the ribosomal sites were stepwise occupied by incubating of re-associated 80S ribosomes with a heteropolymeric MFVK-mRNA and corresponding forms of tRNA (Watanabe, 1972). The heteropolymeric MFVK-mRNA (49 nucleotides long, containing the coding sequence Met-Phe-Val-Lys) was prepared with run-off transcription by using T7 RiboMAX Express Large Scale RNA Production (Promega) according to (Triana et al., 1994). In the first step 80S•mRNA•$tRNA^{Phe}$ complex (0.8 μM), where deacylated $tRNA^{Phe}$ (Sigma) is located in the P site, was formed (2 times excess of tRNA over 80S, incubation 20 min, 37C). In the second step, the A site was filled with N-acetyl-Val-$tRNA^{Val}$ corresponded to the second codon of the MFVK-mRNA (2 times excess tRNA over 80S, incubation 10 min at 37°C). In the third step the $tRNA^{Phe}$ and N-acetyl-Val$tRNA^{Val}$ in the P and A sites, respectively, were translocated to the E and P sites by addition of eEF2 (2 times excess over 80S) and 200 mM GMPPNP (20 min, 37°C). The efficiency of the translocation reaction and the binding state of the tRNAs was determined in a fourth step by means of puromycin reaction (at 37°C, 1 h): puromycin reacts with P-site, but not A-site, bound aminoacyl-tRNA. The occupancy of N-acylated Val-$tRNA^{Val}$ was approximately 0.4 per 80S ribosome and more than 90% of the bound tRNA was reactive to puromycin, indicating a nearly quantitative translocation and P-site location. The complex was prepared just before cryo-grid preparation in a polyamine buffer; 20 mM HEPES pH 7.5, 5 mM $MgCl_2$, 100 mM KCl, 0.6 mM spermine, 0.8 mM spermidine, 6 mM 2-mercaptoethanol.

Grid preparation and cryo-EM—Quantifoil holey carbon grids (Quantifoil Micro Tools GmbH) with a thin carbon layer were glow-discharged in a Plasma Cleaner (PDC002, Harrick). The samples were applied (3.5 µl) and the grid was flash-frozen using a Vitrobot (FEI Company), with a blotting time of 2–4 s. The data was acquired with a Polara Microscope 300 kV (FEI Company) and a K2 Summit DED camera (Gatan) in superresolution mode with a nominal magnification of 31,000×, pixel size = 0.6275 Å, electron dose 30 $e^{-}/Å^{2}$, exposure time 5 s. Images were collected with Leginon (Suloway et al., 2005) at a defocus range of 0.7–3.3 mm.

Data processing and sorting—Initial image processing included Background correction and CTF-calculation (CTFFIND4) (Rohou and Grigorieff, 2015). To account for drift and beam-induced motion during image acquisition, Motioncor 1v.2 (Li et al., 2013) was used to correct the raw micrographs. The obtained micrographs were evaluated with respect to the power spectrum and particle density and in the end, 4097 micrographs were selected for the following reconstruction. Particle images were identified with Signature (Chen and Grigorieff, 2007). After automated particle picking in SPIDER (Frank et al., 1996), 274,077 particle images were used for SPIDER 3D multiparticle Sorting (Frank et al., 1996; Loerke et al., 2010).

SPIDER sorting was initiated with alignment on a density map of an empty 80S ribosome, filtered to ~20 Å, followed by iterative addition of this reference leading to a separation of particle images into ribosome- and noise/junk populations. After separation based on large conformational changes, e.g., 40S subunit rotation, was achieved, focused reassignment on eEF2 was performed (Penczek et al., 2006). 3D variability analysis was used to evaluate the presence/absence of the elongation factor (described in (Behrmann et al., 2015)) and thus the efficiency of the sorting. After obtaining separation into the three populations TI-POST-1, TI-POST-2 and TI-POST 3, PDB-enhancement, small angle alignment and cross-correlation-based recalculation of the CTF-values in SPIDER (Frank et al., 1996) was used to improve the resolution. Additionally, the raw data corresponding to the final dataset was improved by Particle alignment and frame weighting:Particles were realigned individually (Rubinstein and Brubaker, 2015) to correct for anisotropic motion and separate reconstructions were calculated for each frame. From comparison of these reconstructions with an external reference simulated from atomic coordinates, SSNR-based weighting curves were calculated for each frame and all particles were combined using this frame-weighting for the final refinement steps and reconstruction. The local resolution of the density maps was calculated with ResMap using half-maps (Kucukelbir et al., 2014). The unfiltered raw maps from the refinement were filtered to the resolution retrieved from the Fourier shell correlation (FSC) value (0.143) in SPIDER using a Butterworth filter function.

Model-building—As starting point for modeling the mammalian ribosome, the model of the previously published POST-state (PDB: 5aj0) was used (Behrmann et al., 2015). Protein P0 was adapted from the previously published 80S•eEF2 structure PDB: 3j7p (Voorhees et al., 2014). The models of the two tRNAs from PDB: 5aj0 were used and their sequence was corrected in Coot (Emsley and Cowtan, 2004). The mRNA was tentatively built *de novo* in Coot. The model of domains I-III of eEF2 was obtained by a homology model generated by iTasser (Yang et al., 2015) using the yeast eEF2 from PDB: 5it7 as template (Murray et al., 2016). Domains IV and V of eEF2 were adapted from PDB: 3j7p (Voorhees et al., 2014). The models were first fit as rigid bodies with Chimera (Pettersen et al., 2004). If necessary, rRNA domains or helices were separated and docked separately, particularly the L1 stalk, the head and the body/platform. The head was defined as the rRNA C1215-C1685 and the body/platform as A1697–1869 and U1-U1202, while the linking element of h28 was separately docked. For docking of the P-stalk-RNA, MD-Fit was used (Ratje et al., 2010). The separated parts were then re-ligated in Coot. The RNA components of the model were improved with ERRASER (Chou et al., 2013). Then, the model was improved manually with Coot and refined with Phenix real-space refinement (Adams et al., 2010). Manual correction in Coot and refinement in Phenix were repeated iteratively. To avoid overfitting, the weighting for the Phenix refinement was estimated from comparing the cross-resolution curves (Greber et al., 2015): The models were refined with a map comprising half of the particles from the original density map, using different weights. Then density maps were calculated from these refined models. Next, cross resolutions between those maps and both half maps, as well as the corresponding full density map were calculated. The weight was chosen based on evaluation of the cross-resolution curves, focusing on the best compromise between good correlation with respect to the full map and consistency of the curves from cross correlation between the half map used for refinement and the other half map.

Measurement of rotations and figure preparation—40S subunit rotation/rolling and head swivel were measured in chimera using the “measure rotation” command. For the 40S body/ platform, the structures were aligned on the 28S rRNA, and the rotation between a pair of 40S body/platform rRNA (1–1212; 16901869) was measured. For the 40S head, the structures were aligned on the 40S body/platform rRNA, and the rotation between a pair of 40S head rRNA (1210–1690) was measured. The figures of the models were prepared in Chimera (Pettersen et al., 2004).

Nucleotides for smFRET—GTP and GMPPNP were further purified using a Mono Q 5/50 GL anion exchange column (GE Healthcare Life Sciences).

Preparation of fluorescently labeled tRNAs—*E. coli* tRNA^{fMet} and tRNA^{Phe} were purified as previously described (Dunkle et al., 2011; Wang et al., 2011) tRNA^{fMet} was labeled with Cy3 and tRNA^{Phe} with Cy5 at the 4sU8 and acp^3 modifications on nucleotide U47, respectively, as described previously (Blanchard et al., 2004). *E. coli* tRNAs were used for smFRET imaging experiments for reasons discussed previously (Ferguson et al., 2015).

Preparation of mammalian and bacterial complexes for smFRET—Mammalian ribosomal subunits isolated from the polysome fraction of HEK293T cells were used to form 80S initiation complexes as previously described (Ferguson et al., 2015) following a procedure that bypasses the need for exogenous initiation factors (Burgess and Mach, 1971) using purified 40S and 60S subunits, Cy3-labeled Met-tRNA^{fMet} and MFF mRNA (5′-CAA CCU AAA ACU UAC ACA CCC UUA GAG GGA CAA UCG AUG UUU UUU UUU UUU UUU UUU UUU-3′) (Dharmacon) hybridized at the 5′ end to a doublestranded biotinylated DNA linker (5′-GTA AGT TTT AGG TTG CCC CCC TTT TTT TTT TTT

TTT TTT TTT TTT TTT TTT-3′/ 3′-AAA AAA AAA AAA AAA AAA AAA AAA AAA AAA-5′) (IDT).

Wild-type and uS13-labeled initiation complexes were prepared as previously described (Blanchard et al., 2004; Wasserman et al., 2015).

Preparation of ternary complex—Phenylalanine (2.5 mM), PheRS (0.15 mM), pyruvate kinase (0.4 μM), myokinase (0.5 μM), Phosphoenolpyruvate (PEP; 3.75 mM), GTP (630 μM), and Cy5-labeled $tRNA^{Phe}$ (250 nM) were combined in charging buffer (250 mM TRIS pH 8, 100 mM KCl, 500 mM NH_4Cl, 50 mM $MgCl_2$, 5 mM DTT, 12.5 mM ATP, 2.5 mM EDTA) before addition of either eEF1A (1 μM) or EF-Tu•EF-Ts (1 μM). The resulting mixture was incubated for 5 min at 37°C to aminoacylate the tRNA and form ternary complex. Before injection into the microscope flow cell for smFRET imaging, ternary complex was diluted 40X in human polymix buffer containing 0.5 mM GTP to a final concentration of 6.25 nM.

smFRET imaging of mammalian translocation—All smFRET experiments were conducted in human polymix buffer (50 mM TRIS pH 7.5, 5 mM $MgCl_2$, 50 mM NH_4Cl, 2 mM spermidine, 5 mM putrescine) containing a mixture of triplet-state quenchers (1 mM Trolox, 1 mM *4*-nitrobenzyl alcohol (NBA), 1 mM cyclooctatetraene (COT)) (Dave et al., 2009) and an enzymatic oxygen scavenging system (2 μM 3,4-Dihydroxybenzoic acid (PCA), 0.02 U/ml protocatechuate 3,*4*-dioxygenase (PCD)) (Aitken et al., 2008). Surface-immobilized human ribosome pre-translocation complexes were prepared as described previously (Ferguson et al., 2015). Briefly, eEF1A ternary complexes containing Cy5-labeled Phe-$tRNA^{Phe}$ were delivered to surface-immobilized 80S initiation complexes containing P-site Cy3-labeled Met-$tRNA^{fMet}$ and displaying a UUU codon in the A site. Ternary complex was incubated with the ribosomes for 30 s and then washed from the flow cell with human polymix buffer, leading to stoichiometric formation of PRE ribosomes containing Cy3-labeled $tRNA^{fMet}$ in the P site and Cy5-labeled Met-Phe-$tRNA^{Phe}$ in the A site. eEF2 (1 μM) together with either 0.5 mM GTP or GMPPNP was delivered to these PRE complexes by manual injection. smFRET data was recorded using a home-built total internal reflection based fluorescence microscope (Juette et al., 2016) at~0.1 kW/cm^2 laser (532 nm) illumination at a time resolution of 40 ms. Donor and acceptor fluorescence intensities were extracted from the recorded movies and FRET efficiency traces were calculated using custom software implemented in MATLAB R2015b. FRET traces were selected for further analysis according to the following criteria: a single catastrophic photobleaching event, at least 8:1 signal/background-noise ratio and 6:1 signal/signal-noise ratio, less than four donor-fluorophore blinking events, a correlation coefficient between donor and acceptor < 0.5 and a lifetime of at least 50 frames (2 s at 40 ms time resolution) in any FRET state ≥ 0.15.

smFRET imaging of bacterial translocation—All smFRET experiments on bacterial translocation were conducted in the same buffer conditions as the experiments on the human ribosome. Surface-immobilized bacterial PRE complexes were prepared exactly as described (Wasserman et al., 2016). Briefly, EFTu ternary complexes containing Cy5-labeled Phe-$tRNA^{Phe}$ were delivered to surface immobilized 70S initiation complexes containing either

P-site Cy3-labeled fMet-tRNA^{fMet} or P-site fMet-tRNA^{fMet} and N-terminally LD550-labeled ribosomal protein uS13, and displaying a UUU codon in the A site. Ternary complex was incubated with the ribosomes for 30 s and then washed from the flow cell with human polymix buffer, leading to stoichiometric formation of PRE ribosomes containing A-site Cy5-labeled fMet-Phe-tRNA^{Phe} and either unlabeled P-site tRNA^{fMet} and LD550-labeled uS13 or Cy3-labeled P-site tRNA^{fMet}. EF-G (5 μM) together with either 0.5 mM GTP or GMPPNP was delivered to these PRE complexes by manual injection and smFRET data collection was carried out in the same way as for the human ribosome experiments. In the puromycin release experiments 1 mM puromycin pH 7.5 was delivered to the POST complexes by manual injection. FRET between A- and P-site tRNA was monitored at ~0.1 kW/cm^2 laser (532 nm) illumination at a time resolution of 40 ms while FRET between ribosomal protein uS13 and A-site tRNA was monitored at ~0.025 kW/cm^2 laser (532 nm) illumination at a time resolution of 300 ms. Traces were selected for further analysis using the same criteria as in the experiments on the human ribosome.

Analysis of smFRET data and estimation of translocation mean times— smFRET traces were analyzed using hidden Markov model idealization methods as implemented in the SPARTAN software package (Juette et al., 2016). In all idealizations, transitions between all states were allowed. Translocation of the human ribosome was idealized to a five-state model (FRET values: 0.25 ± 0.05, 0.43 ± 0.06, 0.59 ± 0.05, 0.74 ± 0.05 and 0.86 ± 0.05), translocation of the bacterial ribosome from the tRNA-tRNA and uS13-tRNA perspectives was idealized to a three state (FRET values: 0.25 ± 0.05, 0.45 ± 0.07, 0.74 ± 0.05) and a four-state (FRET values: 0.19 ± 0.03, 0.28 ± 0.03, 0.47 ± 0.05, 0.77 ± 0.05) model, respectively. To estimate translocation mean times from the idealized tRNA-tRNA FRET traces, we constructed normalized cumulative distributions over the arrival time to the POST state (0.86 FRET for the human ribosome, 0.74 FRET for the bacterial ribosome). The reaction mean time, was estimated by fitting of a two-exponential function to the data, in all cases the reported mean time corresponds to the time of the major, fast, component making up 85 – 90% of the total amplitude. The mean time of back-translocation of the human ribosome was estimated by fitting of a single-exponential function to a plot of the mean FRET value versus time after washout of eEF2•GMPPNP. The uncertainty in the mean time estimates was calculated by bootstrap analysis.

QUANTIFICATION AND STATISTICAL ANALYSIS

Details of statistical methods used in the various software for cryo-EM data analysis can be found in the relevant original publications. For validation of the atomic models, the pdb-database (https://validate-rcsb-1.wwpdb.org/ and Molprobity (http://molprobity.biochem.duke.edu/) were used.

All smFRET experiments used for quantitative analysis were performed in triplicate. smFRET traces were analyzed using hidden Markov model idealization methods as implemented in the SPARTAN software package (Juette et al., 2016) and reaction mean times were estimated by non-linear fitting. Uncertainties in the estimated mean times were calculated by bootstrap analysis. Uncertainties in the mean times presented in the main text are standard errors. Uncertainties in FRET values estimated from hidden Markov model analysis are standard deviations.

DATA AND SOFTWARE AVAILABILITY

The accession numbers for the cryo-EM density maps reported in this paper are EMDB: EMD-0098 (TI-POST-1 state), EMD-0099 (TI-POST-2 state), and EMD-0100 (TI-POST-3 state). The accession numbers for the atomic coordinates reported in this paper are PDB: 6GZ3 (TI-POST-1 state), 6GZ4 (TI-POST-2 state), and 6GZ5 (TI-POST-3 state).

Supplementary Material

Refer to Web version on PubMed Central for supplementary material.

ACKNOWLEDGMENTS

We thank Thiemo Sprink for his helpful comments and support with interpretation and modeling. The present work was supported by grants from Deutsche Forschungsgemeinschaft (DFG SFB 740 to C.M.T.S.), the NIH (GM079238 to S.C.B. and T32 GM115327-Tan to E.J.R.), and the Swedish Research Council (2017–06313 to M.H.). The authors acknowledge the North-German Supercomputing Alliance (HLRN) for providing high-performance computing resources that have contributed to the research results reported in this paper as well as Roger B. Altman, Daniel S. Terry, and Manuel Juette for support with single-molecule imaging experiments and analysis.

REFERENCES

Abeyrathne PD, Koh CS, Grant T, Grigorieff N, and Korostelev AA (2016). Ensemble cryo-EM uncovers inchworm-like translocation of a viral IRES through the ribosome. eLife 5, 1–31.

Adams PD, Afonine PV, Bunko´ czi G, Chen VB, Davis IW, Echols N, Headd JJ, Hung L-W, Kapral GJ, Grosse-Kunstleve RW, et al. (2010). PHENIX: a comprehensive Python-based system for macromolecular structure solution. Acta Crystallogr. D Biol. Crystallogr 66, 213–221. [PubMed: 20124702]

Adio S, Senyushkina T, Peske F, Fischer N, Wintermeyer W, and Rodnina MV (2015). Fluctuations between multiple EF-G-induced chimeric tRNA states during translocation on the ribosome. Nat. Commun 6, 7442. [PubMed: 26072700]

Agirrezabala X, Lei J, Brunelle JL, Ortiz-Meoz RF, Green R, and Frank J (2008). Visualization of the hybrid state of tRNA binding promoted by spontaneous ratcheting of the ribosome. Mol. Cell 32, 190–197. [PubMed: 18951087]

Aitken CE, Marshall RA, and Puglisi JD (2008). An oxygen scavenging system for improvement of dye stability in single-molecule fluorescence experiments. Biophys. J 94, 1826–1835. [PubMed: 17921203]

Alejo JL, and Blanchard SC (2017). Miscoding-induced stalling of substrate translocation on the bacterial ribosome. Proc. Natl. Acad. Sci. U S A 114, E8603–E8610. [PubMed: 28973849]

Andersen CBF, Becker T, Blau M, Anand M, Halic M, Balar B, Mielke T, Boesen T, Pedersen JS, Spahn CMT, et al. (2006). Structure of eEF3 and the mechanism of transfer RNA release from the E-site. Nature 443, 663–668. [PubMed: 16929303]

Anger AM, Armache JP, Berninghausen O, Habeck M, Subklewe M, Wilson DN, and Beckmann R (2013). Structures of the human and Drosophila 80S ribosome. Nature 497, 80–85. [PubMed: 23636399]

Behrmann E, Loerke J, Budkevich TV, Yamamoto K, Schmidt A, Penczek PA, Vos MR, Bu€rger J, Mielke T, Scheerer P, and Spahn CM (2015). Structural snapshots of actively translating human ribosomes. Cell 161, 845–857. [PubMed: 25957688]

Blanchard SC, Kim HD, Gonzalez RL, Jr., Puglisi JD, and Chu S (2004). tRNA dynamics on the ribosome during translation. Proc. Natl. Acad. Sci. U S A 101, 12893–12898. [PubMed: 15317937]

Bommer U, Burkhardt N, Junemann R, Spahn CMT, Triana-Alonso F, and Nierhaus KH (1997). Ribosomes and polysomes In Subcellular Fractionation: A Practical Approach, Graham J and Rickwood D, eds. (Washington, DC: IRL Press), pp. 271–301.

Bourne HR, Sanders DA, and McCormick F (1991). The GTPase superfamily: conserved structure and molecular mechanism. Nature 349, 117–127. [PubMed: 1898771]

Brilot AF, Korostelev AA, Ermolenko DN, and Grigorieff N (2013). Structure of the ribosome with elongation factor G trapped in the pretranslocation state. Proc. Natl. Acad. Sci. U S A 110, 20994–20999. [PubMed: 24324137]

Budkevich T, Giesebrecht J, Altman RB, Munro JB, Mielke T, Nierhaus KH, Blanchard SC, and Spahn CMT (2011). Structure and dynamics of the mammalian ribosomal pretranslocation complex. Mol. Cell 44, 214–224. [PubMed: 22017870]

Budkevich TV, Giesebrecht J, Behrmann E, Loerke J, Ramrath DJF, Mielke T, Ismer J, Hildebrand PW, Tung CS, Nierhaus KH, et al. (2014). Regulation of the mammalian elongation cycle by subunit rolling: a eukaryotic-specific ribosome rearrangement. Cell 158, 121–131. [PubMed: 24995983]

Burgess AB, and Mach B (1971). Formation of an initiation complex with purified mammalian ribosomal subunits. Nat. New Biol 233, 209–210. [PubMed: 20481011]

Burnett BJ, Altman RB, Ferguson A, Wasserman MR, Zhou Z, and Blanchard SC (2014). Direct evidence of an elongation factor-Tu/ TsGTPAminoacyl-tRNA quaternary complex. J. Biol. Chem 289, 23917–23927. [PubMed: 24990941]

Chen JZ, and Grigorieff N (2007). SIGNATURE: a single-particle selection system for molecular electron microscopy. J. Struct. Biol 157, 168–173. [PubMed: 16870473]

Chen VB, Arendall WB, 3rd, Headd JJ, Keedy DA, Immormino RM, Kapral GJ, Murray LW, Richardson JS, and Richardson DC (2010). MolProbity: all-atom structure validation for macromolecular crystallography. Acta Crystallogr. D Biol. Crystallogr 66, 12–21. [PubMed: 20057044]

Chen J, Petrov A, Tsai A, O'Leary SE, and Puglisi JD (2013). Coordinated conformational and compositional dynamics drive ribosome translocation. Nat. Struct. Mol. Biol 20, 718–727. [PubMed: 23624862]

Chen C, Cui X, Beausang JF, Zhang H, Farrell I, Cooperman BS, and Goldman YE (2016). Elongation factor G initiates translocation through a power stroke. Proc. Natl. Acad. Sci. U S A 113, 7515–7520. [PubMed: 27313204]

Chou F-C, Sripakdeevong P, Dibrov SM, Hermann T, and Das R (2013). Correcting pervasive errors in RNA crystallography through enumerative structure prediction. Nat. Methods 10, 74–76. [PubMed: 23202432]

Connell SR, Takemoto C, Wilson DN, Wang H, Murayama K, Terada T, Shirouzu M, Rost M, Schu €ler M, Giesebrecht J, et al. (2007). Structural basis for interaction of the ribosome with the switch regions of GTP-bound elongation factors. Mol. Cell 25, 751–764. [PubMed: 17349960]

Cornish PV, Ermolenko DN, Noller HF, and Ha T (2008). Spontaneous intersubunit rotation in single ribosomes. Mol. Cell 30, 578–588. [PubMed: 18538656]

Czworkowski J, Wang J, Steitz TA, and Moore PB (1994). The crystal structure of elongation factor G complexed with GDP, at 2.7 A resolution. EMBO J. 13, 3661–3668. [PubMed: 8070396]

Dave R, Terry DS, Munro JB, and Blanchard SC (2009). Mitigating unwanted photophysical processes for improved single-molecule fluorescence imaging. Biophys. J 96, 2371–2381. [PubMed: 19289062]

Dunkle JA, Wang L, Feldman MB, Pulk A, Chen VB, Kapral GJ, Noeske J, Richardson JS, Blanchard SC, and Cate JHD (2011). Structures of the bacterial ribosome in classical and hybrid states of tRNA binding. Science 332, 981–984. [PubMed: 21596992]

Emsley P, and Cowtan K (2004). Coot: model-building tools for molecular graphics. Acta Crystallogr. Sect. D Biol. Crystallogr 60, 2126–2132. [PubMed: 15572765]

Ermolenko DN, and Noller HF (2011). mRNA translocation occurs during the second step of ribosomal intersubunit rotation. Nat. Struct. Mol. Biol 18, 457–462. [PubMed: 21399643]

Ferguson A, Wang L, Altman RB, Terry DS, Juette MF, Burnett BJ, Alejo JL, Dass RA, Parks MM, Vincent CT, and Blanchard SC (2015). Functional dynamics within the human ribosome regulate the rate of active protein synthesis. Mol. Cell 60, 475–486. [PubMed: 26593721]

Frank J, Radermacher M, Penczek P, Zhu J, Li Y, Ladjadj M, and Leith A (1996). SPIDER and WEB: processing and visualization of images in 3D electron microscopy and related fields. J. Struct. Biol 116, 190–199. [PubMed: 8742743]

Gao Y-GY, Selmer M, Dunham CM, Weixlbaumer A, Kelley AC, and Ramakrishnan V (2009). The structure of the ribosome with elongation factor G trapped in the posttranslocational state. Science 326, 694–699. [PubMed: 19833919]

Greber BJ, Bieri P, Leibundgut M, Leitner A, Aebersold R, Boehringer D, and Ban N (2015). The complete structure of the 55S mammalian mitochondrial ribosome. Science 348, 303–308. [PubMed: 25837512]

Inoue-Yokosawa N, Ishikawa C, and Kaziro Y (1974). The role of guanosine triphosphate in translocation reaction catalyzed by elongation factor G. J. Biol. Chem 249, 4321–4323. [PubMed: 4605331]

Jackson RJ, Hellen CUT, and Pestova TV (2010). The mechanism of eukaryotic translation initiation and principles of its regulation. Nat. Rev. Mol. Cell Biol 11, 113–127. [PubMed: 20094052]

Juette MF, Terry DS, Wasserman MR, Altman RB, Zhou Z, Zhao H, and Blanchard SC (2016). Single-molecule imaging of non-equilibrium molecular ensembles on the millisecond timescale. Nat. Methods 13, 341–344. [PubMed: 26878382]

Julián P, Konevega AL, Scheres SHW, Lázaro M, Gil D, Wintermeyer W, Rodnina MV, and Valle M (2008). Structure of ratcheted ribosomes with tRNAs in hybrid states. Proc. Natl. Acad. Sci. USA 105, 16924–16927. [PubMed: 18971332]

Kucukelbir A, Sigworth FJ, and Tagare HD (2014). Quantifying the local resolution of cryo-EM density maps. Nat. Methods 11, 63–65. [PubMed: 24213166]

Li X, Mooney P, Zheng S, Booth CR, Braunfeld MB, Gubbens S, Agard DA, and Cheng Y (2013). Electron counting and beam-induced motion correction enable near-atomic-resolution single-particle cryo-EM. Nat. Methods 10, 584–590. [PubMed: 23644547]

Loerke J, Giesebrecht J, and Spahn CMT (2010). Multiparticle cryo-EM of ribosomes. Methods Enzymol. 483, 161–177. [PubMed: 20888474]

McKinney SA, Joo C, and Ha T (2006). Analysis of single-molecule FRET trajectories using hidden Markov modeling. Biophys. J 91, 1941–1951. [PubMed: 16766620]

Melnikov S, Ben-Shem A, Garreau de Loubresse N, Jenner L, Yusupova G, and Yusupov M (2012). One core, two shells: bacterial and eukaryotic ribosomes. Nat. Struct. Mol. Biol 19, 560–567. [PubMed: 22664983]

Miyauchi K, Ohara T, and Suzuki T (2007). Automated parallel isolation of multiple species of non-coding RNAs by the reciprocal circulating chromatography method. Nucleic Acids Res. 35, e24. [PubMed: 17251194]

Moazed D, and Noller HF (1989). Intermediate states in the movement of transfer RNA in the ribosome. Nature 342, 142–148. [PubMed: 2682263]

Mohan S, and Noller HF (2017). Recurring RNA structural motifs underlie the mechanics of L1 stalk movement. Nat. Commun 8, 14285. [PubMed: 28176782]

Munro JB, Altman RB, O’Connor N, and Blanchard SC (2007). Identification of two distinct hybrid state intermediates on the ribosome. Mol. Cell 25, 505–517. [PubMed: 17317624]

Munro JB, Altman RB, Tung C-S, Sanbonmatsu KY, and Blanchard SC (2010a). A fast dynamic mode of the EF-G-bound ribosome. EMBO J. 29, 770–781. [PubMed: 20033061]

Munro JB, Wasserman MR, Altman RB, Wang L, and Blanchard SC (2010b). Correlated conformational events in EF-G and the ribosome regulate translocation. Nat. Struct. Mol. Biol. 17, 1470–1477. [PubMed: 21057527]

Murray J, Savva CG, Shin BS, Dever TE, Ramakrishnan V, and Fernández IS (2016). Structural characterization of ribosome recruitment and translocation by type IV IRES. eLife 5, 5.

Noller HF, Lancaster L, Zhou J, and Mohan S (2017). The ribosome moves: RNA mechanics and translocation. Nat. Struct. Mol. Biol 24, 1021–1027. [PubMed: 29215639]

Ogle JM, Murphy FV, IV, Tarry MJ, and Ramakrishnan V (2002). Selection of tRNA by the ribosome requires a transition from an open to a closed form. Cell 111, 721–732. [PubMed: 12464183]

Oppenheimer NJ, and Bodley JW (1981). Diphtheria toxin. Site and configuration of ADP-ribosylation of diphthamide in elongation factor 2. J. Biol. Chem 256, 8579–8581. [PubMed: 6267047]

Ortiz PA, Ulloque R, Kihara GK, Zheng H, and Kinzy TG (2006). Translation elongation factor 2 anticodon mimicry domain mutants affect fidelity and diphtheria toxin resistance. J. Biol. Chem 281, 32639–32648. [PubMed: 16950777]

Pellegrino S, Demeshkina N, Mancera-Martinez E, Melnikov S, Simonetti A, Myasnikov A, Yusupov M, Yusupova G, and Hashem Y (2018). Structural insights into the role of diphthamide on elongation factor 2 in mRNA reading-frame maintenance. J. Mol. Biol 430, 2677–2687. [PubMed: 29886014]

Penczek PA, Frank J, and Spahn CMT (2006). A method of focused classification, based on the bootstrap 3D variance analysis, and its application to EF-G-dependent translocation. J. Struct. Biol 154, 184–194. [PubMed: 16520062]

Pestova TV, and Hellen CUT (2003). Translation elongation after assembly of ribosomes on the Cricket paralysis virus internal ribosomal entry site without initiation factors or initiator tRNA. Genes Dev. 17, 181–186. [PubMed: 12533507]

Pettersen EF, Goddard TD, Huang CC, Couch GS, Greenblatt DM, Meng EC, and Ferrin TE (2004). UCSF Chimera—a visualization system for exploratory research and analysis. J. Comput. Chem 25, 1605–1612. [PubMed: 15264254]

Pulk A, and Cate JHD (2013). Control of ribosomal subunit rotation by elongation factor G. Science 340, 1235970. [PubMed: 23812721]

Ramrath DJF, Lancaster L, Sprink T, Mielke T, Loerke J, Noller HF, and Spahn CMT (2013). Visualization of two transfer RNAs trapped in transit during elongation factor G-mediated translocation. Proc. Natl. Acad. Sci. U S A 110, 20964–20969. [PubMed: 24324168]

Ratje AH, Loerke J, Mikolajka A, Brünner M, Hildebrand PW, Starosta AL, Dönhöfer A, Connell SR, Fucini P, Mielke T, et al. (2010). Head swivel on the ribosome facilitates translocation by means of intra-subunit tRNA hybrid sites. Nature 468, 713–716. [PubMed: 21124459]

Rodnina MV, and Wintermeyer W (2011). The ribosome as a molecular machine : the mechanism of tRNA-mRNA movement in translocation. Biochem. Soc. Trans 39, 658–662. [PubMed: 21428957]

Rodnina MV, Savelsbergh A, Katunin VI, and Wintermeyer W (1997). Hydrolysis of GTP by elongation factor G drives tRNA movement on the ribosome. Nature 385, 37–41. [PubMed: 8985244]

Rogg H, Wehrli W, and Staehelin M (1969). Isolation of mammalian transfer RNA. Biochim. Biophys. Acta 195, 13–15. [PubMed: 5357028]

Rohou A, and Grigorieff N (2015). CTFFIND4: fast and accurate defocus estimation from electron micrographs. J. Struct. Biol 192, 216–221. [PubMed: 26278980]

Rubinstein JL, and Brubaker MA (2015). Alignment of cryo-EM movies of individual particles by optimization of image translations. J. Struct. Biol 192, 188–195. [PubMed: 26296328]

Schuwirth BS, Borovinskaya MA, Hau CW, Zhang W, Vila-Sanjurjo A, Holton JM, and Cate JHD (2005). Structures of the bacterial ribosome at 3.5 A resolution. Science 310, 827–834. [PubMed: 16272117]

Selmer M, Dunham CM, Murphy FV, 4th, Weixlbaumer A, Petry S, Kelley AC, Weir JR, and Ramakrishnan V (2006). Structure of the 70S ribosome complexed with mRNA and tRNA. Science 313, 1935–1942. [PubMed: 16959973]

Spahn CM, Gomez-Lorenzo MG, Grassucci RA, Jørgensen R, Andersen GR, Beckmann R, Penczek PA, Ballesta JP, and Frank J (2004). Domain movements of elongation factor eEF2 and the eukaryotic 80S ribosome facilitate tRNA translocation. EMBO J. 23, 1008–1019. [PubMed: 14976550]

Spirin AS (2009). The ribosome as a conveying thermal ratchet machine. J. Biol. Chem 284, 21103–21119. [PubMed: 19416977]

Suloway C, Pulokas J, Fellmann D, Cheng A, Guerra F, Quispe J, Stagg S, Potter CS, and Carragher B (2005). Automated molecular microscopy: the new Leginon system. J. Struct. Biol 151, 41–60. [PubMed: 15890530]

Susorov D, Zakharov N, Shuvalova E, Ivanov A, Egorova T, Shuvalov A, Shatsky IN, and Alkalaeva E (2018). Eukaryotic translation elongation factor 2 (eEF2) catalyzes reverse translocation of the eukaryotic ribosome. J. Biol. Chem 293, 5220–5229. [PubMed: 29453282]

Taylor DJ, Nilsson J, Merrill AR, Andersen GR, Nissen P, and Frank J (2007). Structures of modified eEF2 80S ribosome complexes reveal the role of GTP hydrolysis in translocation. EMBO J. 26, 2421–2431. [PubMed: 17446867]

Tourigny DS, Fernandez IS, Kelley AC, Ramakrishnan V, Fernández IS, Kelley AC, and Ramakrishnan V (2013). Elongation factor G bound to the ribosome in an intermediate state of translocation. Science 340, 1235490. [PubMed: 23812720]

Triana F, Nierhaus KH, and Chakraburtty K (1994). Transfer RNA binding to 80S ribosomes from yeast: evidence for three sites. Biochem. Mol. Biol. Int 33, 909–915. [PubMed: 7987260]

Valle M, Zavialov A, Sengupta J, Rawat U, Ehrenberg M, and Frank J (2003). Locking and unlocking of ribosomal motions. Cell 114, 123–134. [PubMed: 12859903]

Voorhees RM, and Ramakrishnan V (2013). Structural basis of the translational elongation cycle. Annu. Rev. Biochem. 82, 203–236. [PubMed: 23746255]

Voorhees RM, Fernández IS, Scheres SHW, and Hegde RS (2014). Structure of the mammalian ribosome-Sec61 complex to 3.4 Å resolution. Cell 157, 1632–1643. [PubMed: 24930395]

Wang L, Altman RB, and Blanchard SC (2011). Insights into the molecular determinants of EF-G catalyzed translocation. RNA 17, 2189–2200. [PubMed: 22033333]

Wasserman MR, Pulk A, Zhou Z, Altman RB, Zinder JC, Green KD, Garneau-Tsodikova S, Cate JH, and Blanchard SC (2015). Chemically related 4,5-linked aminoglycoside antibiotics drive subunit rotation in opposite directions. Nat. Commun 6, 7896. [PubMed: 26224058]

Wasserman MR, Alejo JL, Altman RB, and Blanchard SC (2016). Multiperspective smFRET reveals rate-determining late intermediates of ribosomal translocation. Nat. Struct. Mol. Biol 23, 333–341. [PubMed: 26926435]

Watanabe S (1972). Interaction of siomycin with the acceptor site of Escherichia coli ribosomes. J. Mol. Biol 67, 443–457. [PubMed: 4558100]

Wilson DN (2009). The A-Z of bacterial translation inhibitors. Crit. Rev. Biochem. Mol. Biol 44, 393–433. [PubMed: 19929179]

Yamamoto H, Unbehaun A, and Spahn CMT (2017). Ribosomal chamber music: toward an understanding of IRES mechanisms. Trends Biochem. Sci 42, 655–668. [PubMed: 28684008]

Yang J, Yan R, Roy A, Xu D, Poisson J, and Zhang Y (2015). The I-TASSER suite: protein structure and function prediction. Nat. Methods 12, 7–8. [PubMed: 25549265]

Zhou J, Lancaster L, Donohue JP, and Noller HF (2013). Crystal structures of EF-G-ribosome complexes trapped in intermediate states of translocation. Science 340, 1236086. [PubMed: 23812722]

Zhou J, Lancaster L, Donohue JP, and Noller HF (2014). How the ribosome hands the A-site tRNA to the P site during EF-G-catalyzed translocation. Science 345, 1188–1191. [PubMed: 25190797]

Highlights

- Translocation intermediates revealed on eEF2-bound mammalian 80S ribosomes
- Inhibition of GTP hydrolysis specifically inhibits final steps of translocation
- E-site tRNA release regulates the reversibility of bacterial and mammal translocation

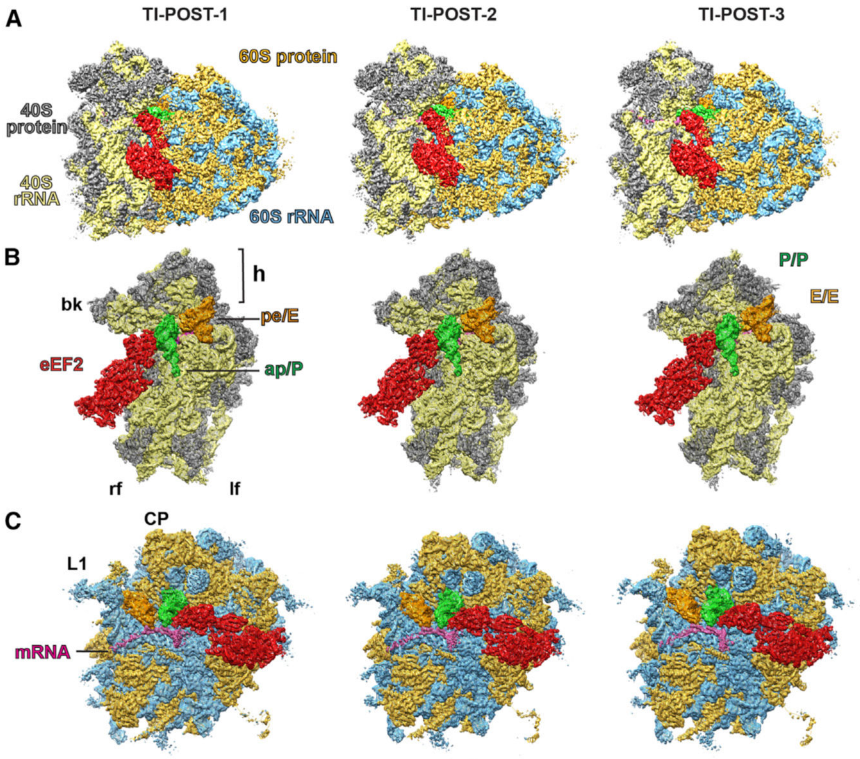

Figure 1. Three Subpopulations of the 80S•tRNA$_2$•eEF2•GMPPNP Complex

Density maps of the three 80S•tRNA$_2$•eEF2•GMPPNP complexes (contour level 2.3σ). 40S rRNA (yellow), 40S proteins (gray), 60S rRNA (blue), 60S proteins (gold), eEF2 (red), ap/P or P/E tRNA (green), pe/E or E/E tRNA (orange), mRNA (pink). Landmarks: 40S head (h), beak (bk), left and right foot (lf, rf), central protuberance (CP), L1 stalk (L1).

(A) Complete 80S density map, view on the intersubunit space.

(B) 40S subunit with eEF2 and tRNA$_2$•mRNA module, view from the intersubunit space.

(C) 60S subunit with eEF2 and tRNA$_2$•mRNA module, view from the intersubunit space.

See also Figure S1 and Table S1.

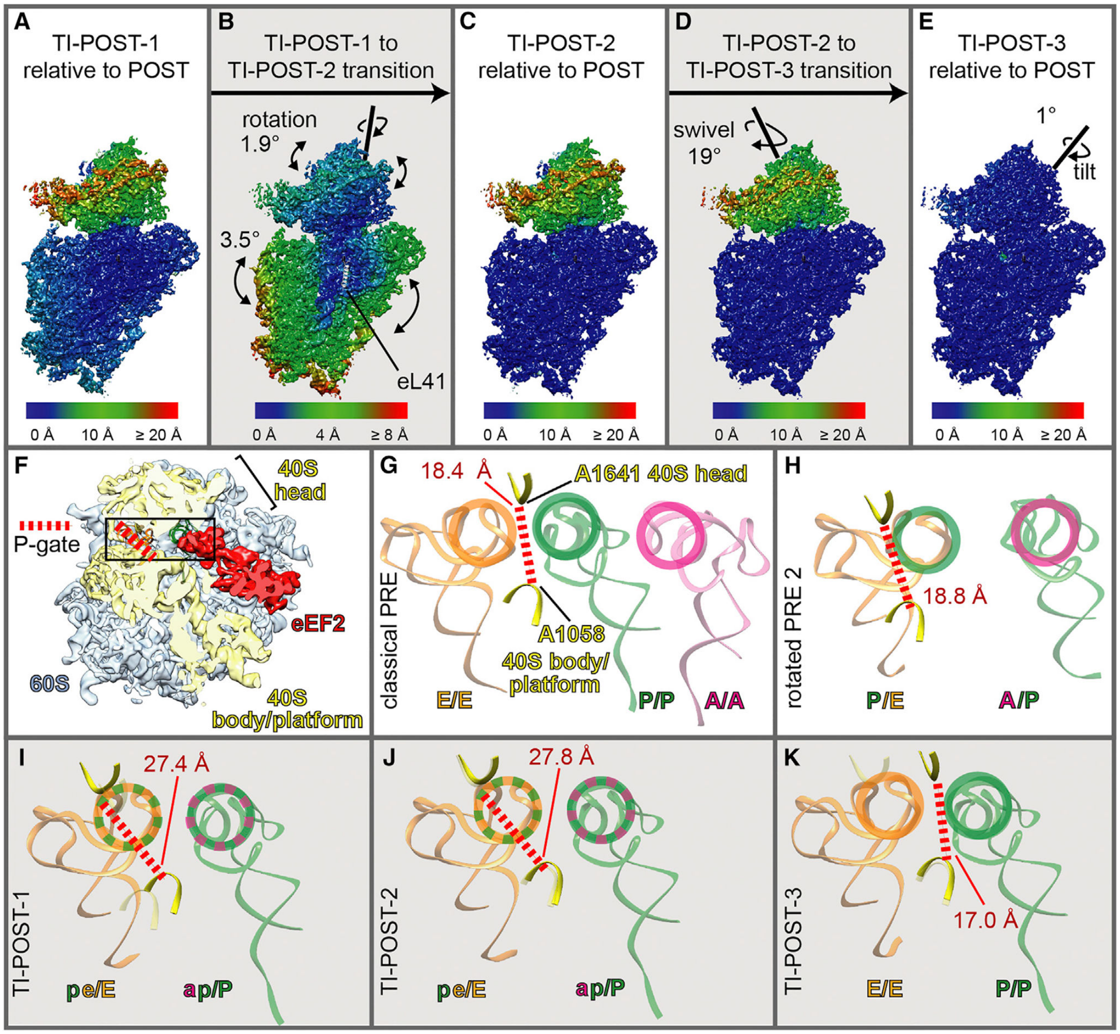

Figure 2. 40S Conformational Changes During Translocation

(A–E) Movement of the 40S. Comparisons are based on a common 60S alignment. Distance changes in the 40S subunit positions resulting from rigid body transformation are color-coded in Å units. Changes of the TI-POST-1 to TI-POST-3 relative to the POST state (PDB: 5AJ0) are shown (A, C, and E) as well as the transitions between TI-POST-1 and TI-POST-2 (B) and between TI-POST-2 and TI-POST-3 (D). Rotation angles and axes were measured in Chimera.

(F) View on the tRNAs in the 40S body/platform-head interface of the TI-POST-1 state from the 40S side. The boxed region containing the P-site gate between A1641, 40S head, and A1058, 40S body/platform is shown in (G)–(K).

(G–K) Opening and closing of the P-site gate during tRNA translocation from the classical PRE state (EMD: 2909; PDB: 3J0O) (Behrmann et al., 2015; Budkevich et al., 2011) (G) via the rotated PRE-2 state (EMD: 2905; PDB: 3J0Q) (Behrmann et al., 2015; Budkevich et al., 2011) (H) and the TI-POST-1 (I), TI-POST-2 (J), and TI-POST-3 (K) states. The colors of the tRNAs correspond to their binding site on the 60S subunit, A (pink), P (green), or E (orange). Circles on top of the tRNA anticodon stem loops show their binding site on the

40S subunit: A (pink), P (green), or E (orange), ap (pink/green), pe (green/orange). Faded cartoons show previous positioning. mRNA is not shown for clarity.

See also Table S2.

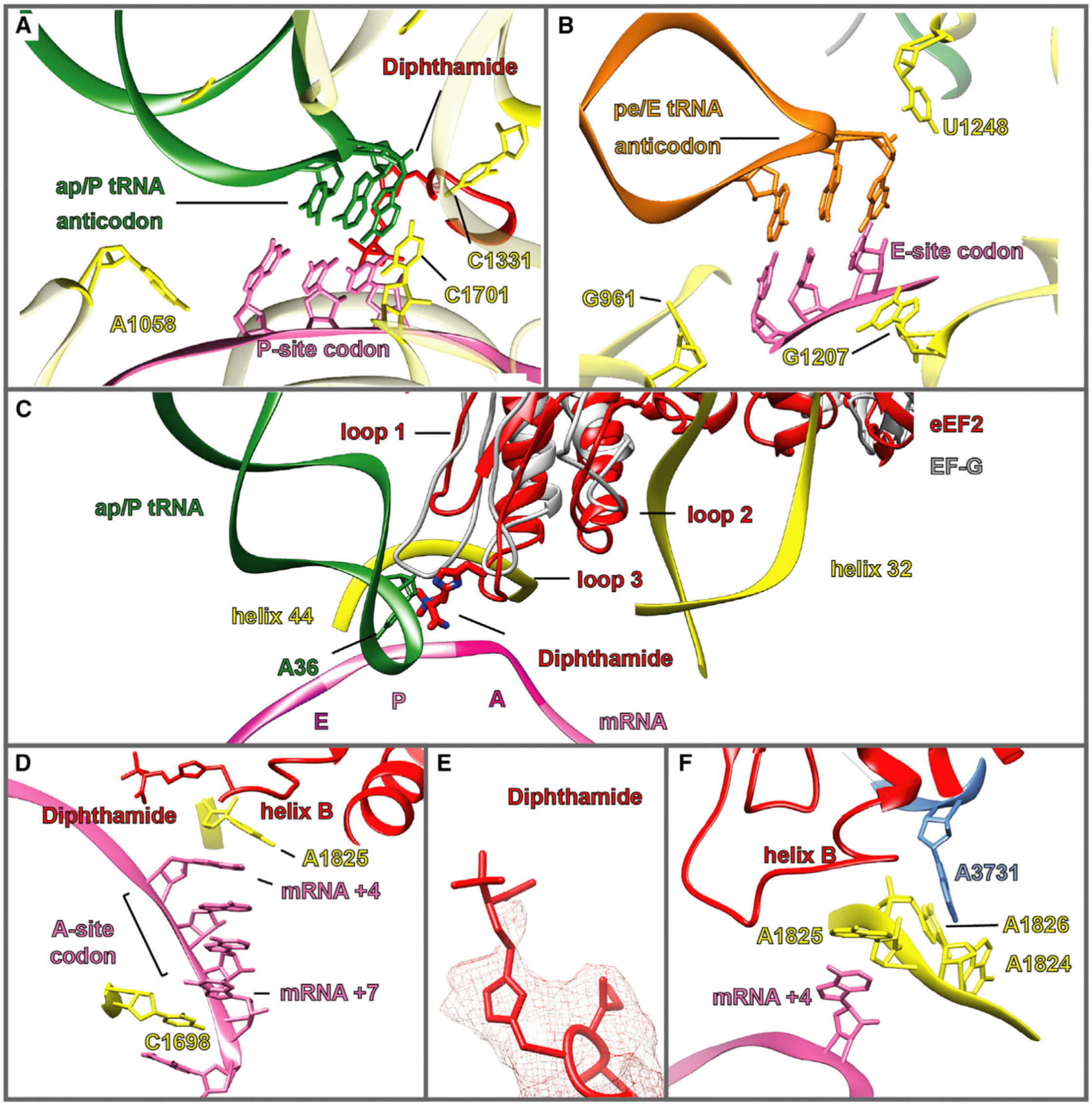

Figure 3. Signature Interactions of the Chimeric Hybrid-State tRNAs, mRNA, and eEF2 on the 40S Subunit in TI-POST-1

40S rRNA (yellow), 60S rRNA (light blue), eEF2 (red), ap/P or P/E tRNA (green), pe/E or E/E tRNA (orange), mRNA (pink), EF-G (gray).

(A and B) Codon-anticodon interactions of ap/P tRNA (A) and pe/E tRNA (B).

(C) Comparison of domain IV of mammalian eEF2 with bacterial EF-G in an alignment via the 23S/28S rRNA. The codons of the mRNA are annotated with A, P, andE and colored differently. The E-site tRNA is not shown for clarity.

(D)Stacked conformation of the A-site codon facilitated by eEF2 helix B and 18S rRNA bases A1825 and C1698.

(E)Density for diphthamide, contour level 1.4σ.

(F)Stabilization of the extruded conformation of A1825 by A3731. Diphthamide removed for clarity.

See also Figure S2.

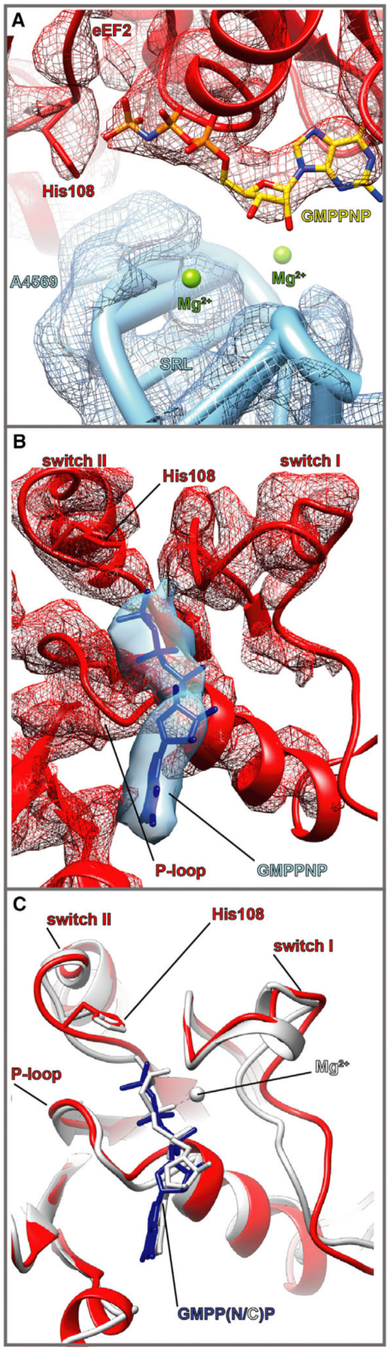

Figure 4. The G Domain of eEF2 in TI-POST-1

(A) Contacts of eEF2 (red) with the SRL (blue). Contour level map 4σ.

(B) Close-up on the GTP pocket. Transparent blue density depicts GMPPNP, red mesh depicts eEF2 (contour level 3σ).

(C) Superposition of the G-domain of eEF2•GMPPNP (red) and the structure of the yeast 80S•IRES•eEF2•GMPPCP complex (PDB: 5IT7; gray) (Murray et al., 2016).

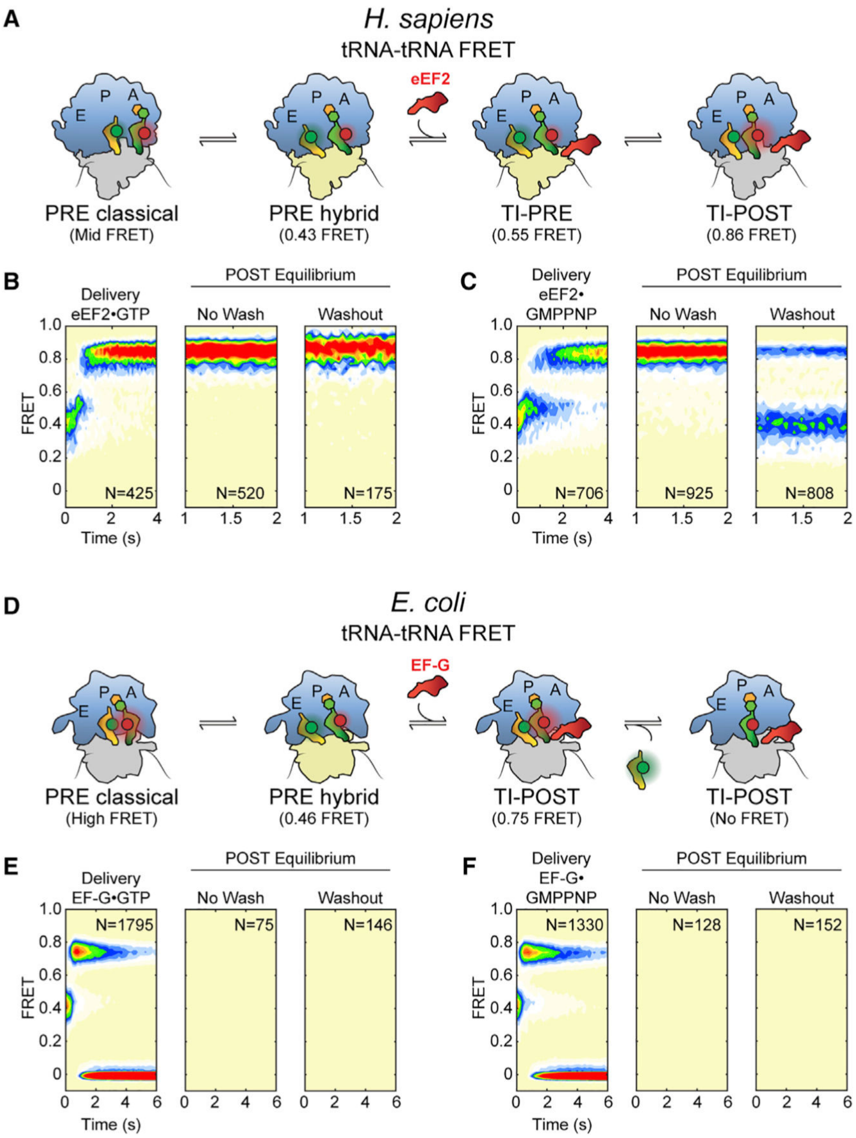

Figure 5. Translocation of the Human and Bacterial Ribosome Observed by smFRET between P- and A-Site tRNAs

(A–F) smFRET studies of translocation by mammalian (A–C) and bacterial (D–F) ribosomes with either GTP (B and E) or GMPPNP (C and F) using a tRNA-tRNA FRET signal.

(A and D) Schematic showing the sites of donor (P-site tRNA, Cy3, green circle) and acceptor (A-site tRNA, Cy5, red circle) fluorescent dyes used to image mammalian translocation (A) or bacterial translocation (D) 60S/50S (blue), unrotated 40S/ 30S (gray), rotated 40S/30S (yellow), deacyl-tRNA (orange), peptidyl-tRNA (green), eEF2/EF-G (dark red).

(B and C) Population FRET histograms showing tRNA-tRNA FRET signal versus time (1) immediately after delivery of eEF2•GTP (B) or eEF2•GMPPNP (C), (2) after translocation while eEF2 is still present in the flow cell, and (3) 30 min after washout of eEF2 from the flow cell.

(E and F) Population FRET histograms showing tRNA-tRNA FRET signal versus time (1) immediately after delivery of EF-G•GTP (E) or EF-G•GMPPNP (F), (2) after translocation while EF-G is still present in the flow cell, and (3) 30 min after washout of EF-G from the flow cell. For clarity of presentation, only traces exhibiting FRET below 0.6 prior to EF-G injection are shown.

See also Figure S3.

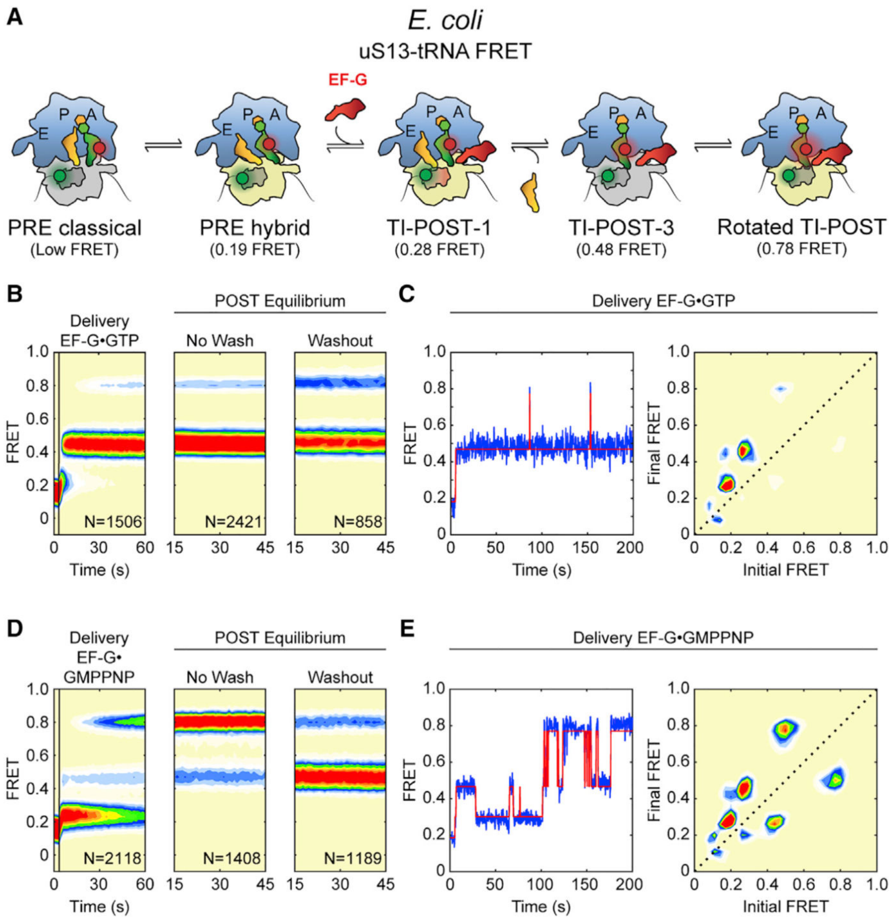

Figure 6. Translocation of the Bacterial Ribosome Observed by smFRET between Ribosomal Protein uS13 and A-Site tRNA

(A) Schematic showing the sites of donor (uS13 N terminus, LD550, green circle) and acceptor (A-site tRNA, Cy5, red circle) fluorescent dyes used to imagetranslocation in (B)–(E). Colors as in Figure 5D, unswiveled 30S head (dark gray), swiveled 30S head (salmon).

(B)Population FRET histograms showing uS13-tRNA FRET signal versus time, (1) immediately after delivery of EF-G•GTP (indicated by a vertical black line), (2) after translocation while EF-G is present in the flow cell, and (3) after washout of EF-G from the flow cell.

(C and E) Illustrative smFRET trace in blue with idealized model in red (left) and transition density plot (right) showing the transitions between different FRET states during translocation with EF-G•GTP (C, corresponding to B, panel 1) or EF-G•GMPPNP (E, corresponding to D, panel 1).

(D) Population FRET histograms showing uS13-tRNA FRET signal versus time after delivery of EF-G•GMPPNP as in (B).

See also Figure S4.

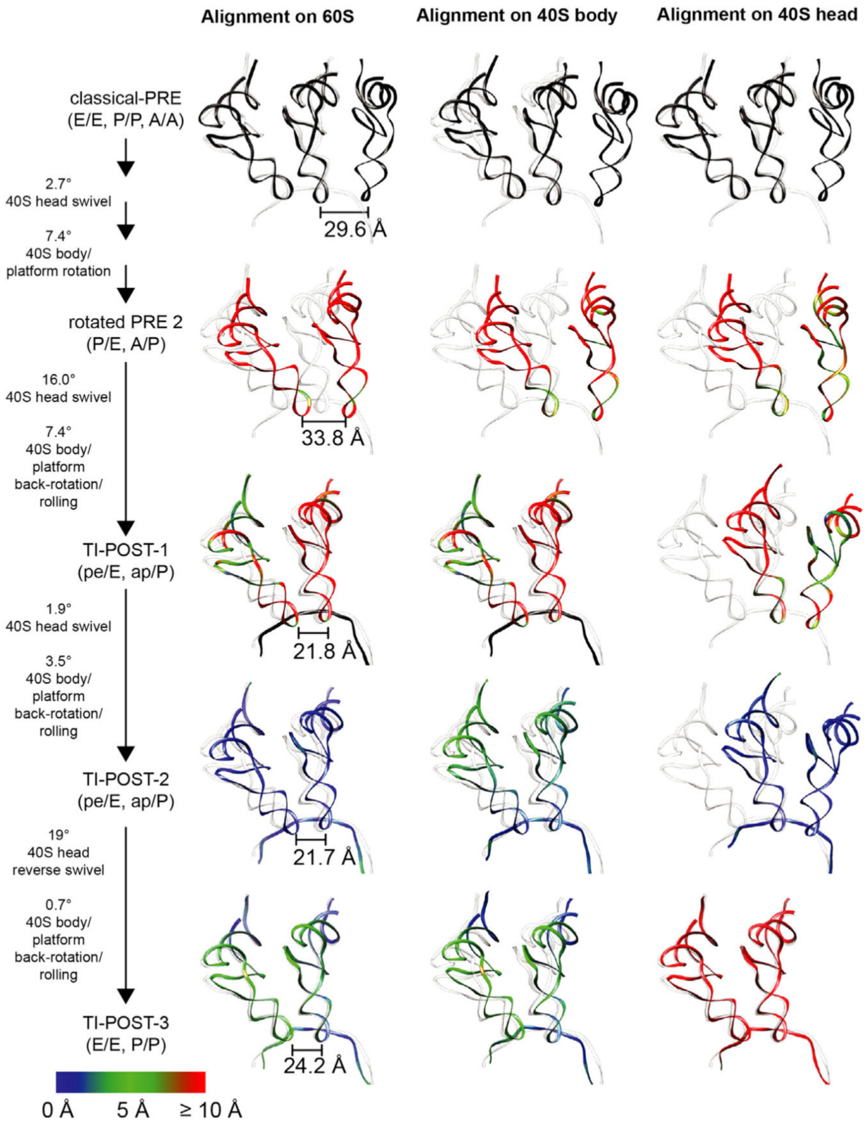

Figure 7. The Path of the tRNAs during Mammalian Translocation

tRNA positions during translocation, relative to the 60S subunit (left), 40S body/platform (middle), and 40S head (right). The color code represents the distance between the atoms compared with the previous step. POST-state tRNAs are depicted in gray in all panels. For the 60S alignment (left) the distance between nucleotides 31 of the tRNAs is denoted to show the compaction and decompaction of the $tRNA_2$•mRNA module. The legend on the left describes the conformational changes from state to state. 40S body/platform rotation (or rolling) is measured relative to the 60S subunit, while 40S head swivel is relative to the 40S body/ platform.

See also Figure S5.

KEY RESOURCES TABLE

REAGENT or RESOURCE	**SOURCE**	**IDENTIFIER**
Bacterial and Virus Strains		
E. coli commercial One Shot MAX Efficiency DH10B T1 Phage-Resistant Cells	ThermoFisher Scientific	Cat#12331013
E. coli commercial One Shot BL21(DE3) Chemically Competent cells	ThermoFisher Scientific	Cat#C600003
Biological Samples		
Yeast $tRNA^{Phe}$	Sigma	Cat#R4018
Rabbit reticulocyte lysate (RRL)	Green Hectares	N/A
Chemicals, Peptides, and Recombinant Proteins		
ATP	Sigma-Aldrich	Cat#FLAAS
Complete, EDTA-free Protease Inhibitor Cocktail	Sigma-Aldrich	Cat#11873580001
LD550	Lumidyne Technologies	Cat#LD550
LD650	Lumidyne Technologies	Cat#LD650
Cy3	Synthesized in house	N/A
Cy5	Synthesized in house	N/A
EcoRI	NEB	Cat#R0101
GTP	Sigma-Aldrich	Cat#G8877
GMPPNP	Sigma-Aldrich	Cat#G0635
Mammalian ProteaseArrest protease inhibitor	G-Biosciences	Cat#786–331
Myokinase	Sigma-Aldrich	Cat#M5520
Phenol water saturated, pH 6.6	Ambion	Cat#AM9712
Phosphoenolpyruvate (PEP)	Sigma-Aldrich	Cat#P7127
Puromycin (dihydrochloride)	Sigma-Aldrich	Cat#58–58-2
Pyruvate Kinase	Sigma-Aldrich	Cat#P9136
RNasin® Plus	Promega	Cat#N2611
Valine, L-[^{14}C(U)]	PerkinElmer	Cat#NEC291E
3,4-Dihydroxybenzoic acid (PCA)	Sigma-Aldrich	Cat#37580
4-nitrobenzyl alcohol (NBA)	Sigma-Aldrich	Cat#N12821
Cyclooctatetraene (COT)	Sigma-Aldrich	Cat#138924
Protocatechuate *3,4*-dioxygenase (PCD)	Sigma-Aldrich	Cat#P8279–25UN
Trolox	Sigma-Aldrich	Cat#238813
Critical Commercial Assays		
T7 RiboMAX Express Large Scale RNA Production	Promega	Cat#P1320
Deposited Data		
Cryo-EM density map: TI-POST-1 state	This study	EMD-0098

REAGENT or RESOURCE	SOURCE	IDENTIFIER
Cryo-EM density map: TI-POST-2 state	This study	EMD-0099
Cryo-EM density map: TI-POST-3 state	This study	EMD-0100
Model: TI-POST-1 state	This study	PDB ID: 6GZ3
Model: TI-POST-2 state	This study	PDB ID: 6GZ4
Model: TI-POST-3 state	This study	PDB ID: 6GZ5
Experimental Models: Cell Lines		
HEK293T	ATCC	Cat#CRL-3216; RRID:CVCL_0063
Oligonucleotides		
MFF mRNA (5′-CAA CCU AAA ACU UAC ACA CCC UUA GAG GGA CAA UCG AUG UUU UUU UUU UUU UUU UUU UUU-3′)	Dharmacon	N/A
Recombinant DNA		
biotinylated dsDNA (5′-GTA AGT TTT AGG TTG CCC CCC TTT TTT TTT TTT TTT TTT TTT TTT TTT TTT-3′/ 3′-AAA AAA AAA AAA AAA AAA AAA AAA AAA AAA-5′)	Dharmacon	N/A
DNA oligo for tRNA^{Val} purification 5′ - TgTTT CCgCCCggTTTCgAACCggggACCT-BIO	TIB MolBiol	N/A
Software and Algorithms		
SPARTAN	(Juette et al., 2016)	version 3.3.0
Leginon	(Suloway et al., 2005)	http://leginon.org
CTFFIND4	(Rohou and Grigorieff, 2015)	http://grigoriefflab.janelia.org/ctffind4
SIGNATURE	(Chen and Grigorieff, 2007)	http://grigoriefflab.janelia.org/signature
SPIDER	(Frank et al., 1996)	https://spider.wadsworth.org/
ResMap	(Kucukelbir et al., 2014)	http://resmap.sourceforge.net/
MotionCorr1v.2	(Li et al., 2013)	http://msg.ucsf.edu/em/software/ (Only newer version (Motioncor2) available now)
Chimera	(Pettersen et al., 2004)	https://www.cgl.ucsf.edu/chimera/
Coot	(Emsley and Cowtan, 2004)	http://www2.mrc-lmb.cam.ac.uk/Personal/pemsley/coot/
MDfit	(Ratje et al., 2010)	http://sanbonmatsu.org/gmx-4.5.5mdfit.tar.gz
PHENIX	(Adams et al., 2010)	https://www.phenix-online.org/
iTasser	(Yang et al., 2015)	https://zhanglab.ccmb.med.umich.edu/ I-TASSER/
ERRASER	(Chou et al., 2013)	https://www.rosettacommons.org/manuals/archive/rosetta3.4_user_guide/index.html
Molprobity	(Chen et al., 2010)	http://molprobity.biochem.duke.edu/
RCSB PDB Validation service		https://validate-rcsb-1.wwpdb.org/
SPARTAN	(Juette et al., 2016)	version 3.3.0

REAGENT or RESOURCE	SOURCE	IDENTIFIER
Other		
Mono Q HR 5/5 FPLC column	GE Healthcare	Cat#17–0546-01
P11 phosphocellulose	Sigma-Aldrich	Cat#C3145
HiTrap Heparin HP column	GE Healthcare	Cat#17040701
Nucleosil 300–7 C8 HPLC column	Knauer	Cat#25DK089NSL
Streptavidin Sepharose HP	GE Healthcare	Cat#90100484
SP-Sepharose, Fast flow	GE Healthcare	Cat#GE17–0729-10
Carbon coated holey grids (2nm) R 3/3 Copper	Quantifoil	N/A
tRNA sequences		http://trna.bioinf.uni-leipzig.de
rRNA secondary structure maps		http://jufali.userpage.fu-berlin.de http://www.rna.icmb.utexas.edu/